

THESIS FOR THE DEGREE OF LICENTIATE OF ENGINEERING

Functionalization and Characterization of Carbon-based Nanomaterials

Nan Wang



CHALMERS

Department of Microtechnology and Nanoscience (MC2)

BioNano Systems Laboratory

CHALMERS UNIVERSITY OF TECHNOLOGY

Göteborg, Sweden 2015

Functionalization and Characterization of Carbon-based Nanomaterials

Nan Wang

© 2015 Nan Wang

Department of Microtechnology and Nanoscience (MC2)

BioNano Systems Laboratory (BNSL)

ISSN 1652-0769

Technical report no MC2- 314

Chalmers University of Technology

Department of Microtechnology and Nanoscience (MC2)

BioNano Systems Laboratory (BNSL)

SE-412 96 Göteborg, Sweden

Telephone +46 (0)31-772 1000

Printed by Chalmers Reproservice

Göteborg, Sweden 2015

Abstract

Surface functionalization of nanomaterials opens up unlimited possibilities to combine the distinct properties of inorganic, organic, or even bioactive components in a single material and bring novel functionalities in a wide range of applications ranging from electronics to catalysts and medicine carriers. So far, a variety of organic and inorganic nanomaterials have been explored to construct different functionalized nanomaterials. Among them, carbon nanomaterials (CNMs), such as carbon nanotubes (CNTs) carbon nanofibers (CNFs) and graphene, are believed to be promising building blocks for constructing nanoscale functionalized materials, owing primarily to their large surface area and extraordinary electrical and mechanical properties. In this thesis, flexible and scalable chemical approaches to functionalize CNMs are developed for different applications. According to the bonding difference between CNMs and the functional components, these approaches can be divided into two groups, including covalent functionalization and non-covalent functionalization. In addition, a variety of characterization methods are utilized to characterize the structures and properties of the as-fabricated functionalized CNMs.

Covalent functionalization of CNMs surface is based on reactions with the oxygen-containing groups of CNMs which are bonded directly to the π -conjugated skeleton of the CNMs. The first part of the work in the thesis is to functionalize CNTs surface via simultaneously oxidation and ultrasonication treatments and fabricate metal nanoparticle decorated CNT hybrid. As a result, finely grained and uniform silver nanoparticles were successfully deposited on the surface of activated CNTs. The other part of covalent functionalization of CNMs is about the fabrication of free-standing graphene based films (GBFs) via self-assembly and functionalization to improve GBF's heat spreading performance. The results show efficient cooling performance of the functionalized GBF which could offer potential solutions for the thermal management of high power devices.

Non-covalent functionalization utilizes various functional molecules or active species as assembly mediators to functionalize the surface of CNMs via non-covalent interactions. In the thesis, non-covalent functionalization of CNTs was realized through polymer wrapping. The targeted wrapping of APTES and silica layers on the surface of CNTs enabled homogeneous CNT dispersion in various polar solvents, and also facilitated the silver nanoparticle's deposition. The synthesized multi-functionalized CNT based hybrid nanowires demonstrated superior mechanical and electrical performance in the application of flexible and stretchable circuits (FSCs) due to a highly conductive and flexible structure, which show great potential in the field of wearable and portable electronics.

Keywords: carbon nanomaterials, functionalization, graphene, flexible electronics, hybrid nanowires

List of Publications

Appended papers

This thesis is based on the following appended papers:

A Efficient Surface Activation of Carbon Nanotubes for Synthesis of Highly Uniform Silver Nanoparticles

Nan Wang, Lilei Ye, Murali Murugesan, Johan Liu

In manuscript

B Improved Heat Spreading Performance of Functionalized Graphene in Micro electronic Device Application

Yong Zhang, Haoxue Han, Nan Wang, Pengtu Zhang, Yifeng Fu, Murali Murugesan, Michael Edwards, Kjell Jeppson, Sebastian Volz, Johan Liu

Journal Paper – Advanced Functional Materials published online: 5 JUN 2015. DOI: 10.1002/adfm.201500990

C Flexible Multi-functionalized Carbon Nanotubes Based Hybrid Nanowires

Nan Wang, Di Jiang, Lilei Ye, Murali Murugesan, Michael Edwards, Yifeng Fu, Johan Liu

Journal Paper –Advanced Functional Materials 2015, 25, 26:4135–4143 (DOI: 10.1002/adfm.201501017)

Other contributions

The following selection of contributions is appended to the thesis due to overlap or being outside of the scope of the thesis:

A Thermal characterization of power devices using graphene-based film

Pengtu Zhang, Nan Wang, Carl Zandén, Lilei Ye, Yifeng Fu, Johan Liu
Proceedings – 2014 64th IEEE Electronic Components and Technology Conference (ECTC) 459–463. doi:10.1109/ECTC.2014.6897324

B Development and characterization of graphene-enhanced thermal conductive adhesives

Marcello Casa, Nan Wang, Huang Shirong, Lilei Ye, Ciambelli Paolo, Johan Liu
Proceedings – 2014 15th International Conference on Electronic Packaging Technology (ICEPT) 480–483. doi:10.1109/ICEPT.2014.6922700

C Use of graphene-based films for hot spot cooling

Yong Zhang, Pengtu Zhang, Nan Wang, Yifeng Fu, Johan Liu
Proceedings of the 5th Electronics System-Integration Technology Conference, ESTC 2014 p. Art. no. 6962834. (2014)

D Reliability investigation of nano-enhanced thermal conductive adhesives

Nan Wang, Murali Murugesan, Lilei Ye, Björn Carlberg, Si Chen, Johan Liu
Proceedings – of the 2012 12th IEEE Conference on Nanotechnology, doi:10.1109/NANO.2012.6322137

Abbreviations

CNT	Carbon Nanotube
ED	Ethylenediamine
EDTA	Ethylenediaminetetraacetic acid
PVP	polyvinylpyrrolidone
APTES	(3-Aminopropyl)triethoxysilane
PDMS	Polydimethylsiloxane
TEM	Transmission electron microscopy
SEM	Scanning Electron Microscopy
FT-IR	Fourier transform infrared spectroscopy
XRD	X-ray diffraction
UV	Ultra violet
FSCs	Flexible and stretchable circuits
LED	Light-emitting diode
TGA	Thermogravimetric analysis
BET	Brunauer-Emmett-Teller
BJH	Barrett-Joyner-Halenda
GO	Graphene oxide
GBF	Graphene based film

Table of Contents

Abstract	I
List of Publications.....	II
Chapter 1 Introduction	1
1.1 Nanomaterials.....	1
1.2 Carbon-based nanomaterials	2
1.3 Functionalization of CNMs	3
1.4 Scope and outline	6
Chapter 2 Covalent Functionalization of CNMs.....	7
2.1 Covalent assembly of silver coated CNTs hybrids	7
2.1.1 Surface activation of CNTs	8
2.1.2 Deposition of silver nanoparticles on the activated CNTs.....	12
2.2 Covalent functionalization of GBF for improving its cooling property.....	15
2.2.1 Graphene for hotspot cooling	15
2.2.2 Fabrication of GBFs	15
2.2.3 Functionalization of GBFs for improving its cooling performance	17
Chapter 3 Non-covalent Functionalization of CNMs	20
3.1 Multi-functionalized CNT based hybrid nanowires.....	20
3.1.1 Functionalization of CNT surface by APTES and SiO ₂	21
3.1.2 Deposition of silver nanoparticles on the functionalized CNTs	23
3.2 Fabrication of flexible and stretchable electrical circuits.....	26
3.2.1 Flexible and stretchable circuits	26

3.2.2	Patterning and fabrication of high-resolution FSCs	26
3.3	Electro-mechanical properties and reliability of FSCs	30
3.3.1	Electrical resistivity change of FSCs as a function of silver coverage ratios	30
3.3.2	Flexibility and reliability of FSCs	32
3.3.3	Stretchability and reliability of FSCs	34
3.4	Improved stretchability and reliability of FSCs	36
Chapter 4 Conclusions and Outlook		39
Acknowledgements.....		41
Bibliography.....		42

Chapter 1

Introduction

1.1 Nanomaterials

Nanotechnology, as an emerging/enabling technology, is helping to considerably improve, even revolutionize, many traditional technologies and industry areas, ranging from electronic packaging to energy conversion and storage[1]–[8], from additives to catalysis[9]–[11], and from sensors to drug delivery and biomedical applications[12]–[17]. Driven by the great benefits from these applications, all kinds of research based on nanotechnologies have been carried out in multi-disciplinary areas. In order to distinguish this new technology from the traditional disciplines, the generalized definition of nanotechnology was subsequently established by the National Nanotechnology Initiative, which describes nanotechnology as the manipulation of materials with at least one dimension sized from 1 to 100 nanometers[18]. The reason for such a definition is that most fundamental physical properties of materials can change when the geometry size is reduced to a critical value well below 100 nm in at least one dimension. Table 1.1 shows an overview of the effects and potential applications of the reduced dimensionality of nanomaterials[19].

A variety of nanomaterials have been fabricated and applied in many areas. Generally, nanomaterials can be classified into four groups according to their structural dimensions[20]. As shown in Figure 1.1, zero-dimensional (0D) nanomaterials means that materials are nanoscale in all dimensions, including all kinds of nanoparticles ranging from metal to ceramic. One dimensional (1D) nanomaterials are described as materials which have one dimension larger than nanoscale, such as nanowires and nanotubes. Among them, carbon nanotubes (CNT), including single-walled carbon nanotubes (SWCNT) and multi-walled

Table 1.1 an overview of the effects and potential applications of the reduced dimensionality of nanomaterials

Nanoscale effects	Applications
High surface-to-volume ratio and enhanced reactivity	Catalysis, solar cells, batteries, gas sensors
Enhanced electrical properties	Conducting materials
Increased hardness from small crystal grain size	Hard coatings, thin protection layers
Narrower electronic band gap	Opto-electronics
Lower melting and sintering temperatures	Processing of materials, low sintering materials
Improved transport kinetics	Batteries, hydrogen storage
Improved reliability	Nanoparticle-encapsulated electronic components
Increased wear resistance	Hard coatings, tools
Higher resistivity with smaller grain size	Electronics, passive component, sensors

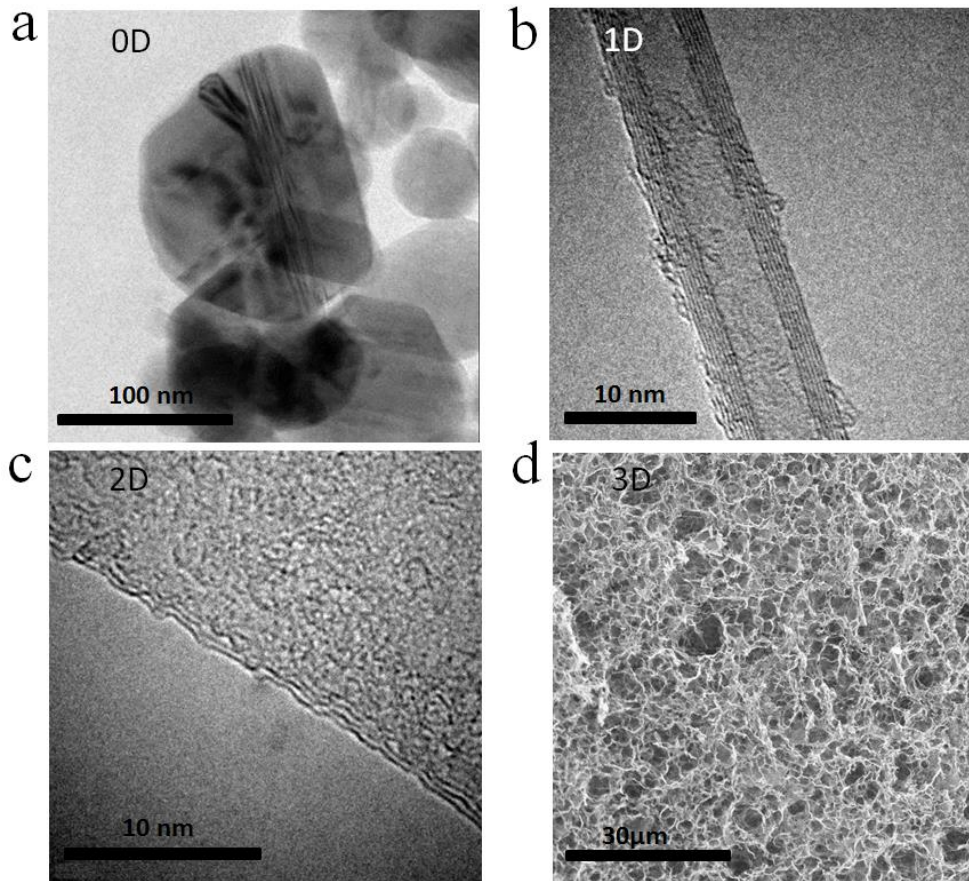


Figure 1.1 Different types of nanomaterials classified by structural dimensions (a) 0D silicon carbide nanoparticles (b) 1D multi-walled carbon nanotube (c) 2D multilayer graphene (d) 3D graphene sponge

carbon nanotubes (MWCNTs), are the most representative 1D nanomaterial. Two-dimensional (2D) nanomaterials usually refer to thin-sheet materials with nanoscale thickness. For example, graphene, one or few layers of carbon atoms, have been regarded as one of the most promising 2D nanomaterials. Three-dimensional (3D) nanomaterials usually include powders, fibrous, multilayer and polycrystalline materials which are constructed by all kinds of building blocks, such as 0D, 1D and 2D nanomaterials. The building blocks are in close contact with each other and form interfaces inside 3D nanomaterials. Figure 1.1d shows the 3D graphene sponge in which individual graphene sheet are bonded together through self-assembly. This special 3D structure has the advantages of large surface area and extremely low density, making it a promising material for supercapacitors[21].

1.2 Carbon-based nanomaterials

Carbon is well known to form distinct solid state allotropes with diverse structures ranging from sp^3 bonded diamond to sp^2 bonded fullerene and graphite. Mixed states are also possible and form the basis of amorphous carbon[22]. The diversity of carbon-lattice structures can lead to great differences on bulk properties ranging from mechanical strength to electrical and thermal performance. Diamond is a metastable form of carbon that possesses a face-centered

cubic lattice structure with a lattice constant of 3.57 Å and C–C bond length of 1.54 Å. Such extremely rigid lattice structure endows diamond with superlative physical qualities, such as the highest hardness and thermal conductivity of all the bulk material[23]. In contrast, graphite is the most thermodynamically stable form of carbon under normal conditions and consists of a layered planer structure where the carbon atoms are arranged in a hexagonal honeycomb lattice with a bond length of 1.42 Å. These single atom thick layers (i.e., graphene layers) are bonded via noncovalent van der Waals forces with an interlayer spacing of 3.35 Å. Such a special layered two-dimensional structure would benefit the phonon transfer in horizontal direction by giving a large group velocity and long mean free path. Consequently, graphite shows superior in-plane thermal and electrical conductivities which facilitate its widespread application in thermal management and electrodes[24]. In addition, the loose interlamellar coupling between graphene layers makes graphite to be an excellent lubricant that has been widely used in industry[25].

The weak interlayer bonding in graphite implies that graphite can be exfoliated and engineered to various types of carbon-based nanomaterials (CNM), including fullerenes, single or multi-walled nanotubes and graphene. Fullerenes are the zero-dimensional form of graphitic carbon that can be visualized as an irregular sheet of graphene being curled up into a sphere by incorporating pentagons in its structure. The first fullerene molecule was discovered in 1985 and named as buckminsterfullerene (C₆₀) which is the smallest fullerene molecule containing pentagonal and hexagonal rings. Nowadays, fullerene molecules come in various forms and sizes ranging from 30 to 3000 carbon atoms, which have been widely researched in lots of areas, such as solar cells, superconductors, x-ray imaging contrast agents and drug delivery[26]–[29].

Among all kinds of CNMs, CNTs and graphene are the most popular 1D and 2D nanomaterials that have been extensively studied in the past two decades. Comprising of a sp^2 bonded hexagonal graphitic structure, CNTs and graphene both possess excellent mechanical strength, electrical and thermal conductivity, and optical properties. The Young's modulus and tensile strength of a CNT and graphene can reach to 1 TPa and 130 GPa[30]. Electron mobility of graphene is more than $15000 \text{ cm}^2 \cdot \text{V}^{-1} \cdot \text{s}^{-1}$, and the current density of metallic CNTs are orders of magnitude higher than those of metals such as copper[31], [32]. Thermal conductivities of a single CNT and graphene are about 3000 W/mK and 5000 W/mK respectively[33]. The light absorption ratio of single-layer graphene is just 2.5%[34]. Lots of the research efforts have been focused on utilizing these advantageous properties for various applications including electronics, biological engineering, filtration, lightweight/strong composite materials, photovoltaics and energy storage[35]–[38].

1.3 Functionalization of CNMs

Surface functionalization of nanomaterials refer to assemble different organic and inorganic materials together in nanoscale through covalent bonds or non-covalent bonds including hydrogen bonds, the electrostatic force, or the van der Waals force[39]. The unlimited possible combinations of the distinct properties of inorganic, organic, or even bioactive components have attracted considerable attention[40]–[42]. So far, a vast number of novel

advanced functionalized CNMs with well-controlled structures and multiple functions have been created and applied in many fields. For example, flexible electrode materials consisting of highly electrically conductive metal nanoparticles coated CNTs demonstrate collective properties of high current density and good flexibility[43]. Graphene coated with ferromagnetic nanoparticles exhibit controlled movement under magnetic fields, demonstrating great potential for magnetic recording[44]. In particular, CNTs deposited with catalytic nanoparticles, such as Pt, Pd and Ru, may provide high-performance catalysts for applications in fuel cell electrodes, Li-ion batteries and supercapacitors[45]–[47].

A variety of physical and chemical approaches have been developed to controllably design and functionalize CNMs with different functional components at the nanoscale[48]–[52]. Generally, these functional routes can be divided into two types, including covalent functionalization and non-covalent functionalization, according to the different connection mechanisms between CNMs with the functional components.

The covalent functionalization is based on forming covalent bonds between functional components and carbon atoms in the basal plane of CNMs[53]. Due to the chemically inert and hydrophobic properties of graphite, it is usually difficult to directly assemble functional components on the surface of CNMs. Therefore, the covalent functionalization of CNMs is necessary for fabrication of CNM-enhanced composites. During the functionalization, a vast number of oxygen-containing groups, such as carbonyl and carboxyl groups, would be grafted onto the graphitic surfaces and form covalent bonds to the p-conjugated skeleton of CNMs under aggressive conditions (e.g., strong acid oxidation or plasma etching)[54], [55]. These oxygen-containing groups show high reactivity with many other functional nanomaterials and also possibly act as attaching points for further assembling of nanohybrids.

However, in most cases, the covalent functionalization processes unavoidably cause the destruction of the graphitic structures, and thus compromise their intrinsic electronic and mechanical properties. Therefore, there is a growing interest in the development of non-covalent interactions between the CNMs and functional components. The principle ideas of non-covalent assembly are to utilize various functional molecules or active species as assembly mediators to functionalize the surface of CNMs via non-covalent interactions such as hydrophobic[56], π - π stacking[57], and wrapping interactions[58], [59]. The assembled mediators then act as binding points for anchoring other molecules or nanomaterials.

Previous research has revealed the chemical mechanisms behind different methods of non-covalent functionalization. The first method, hydrophobic interaction, utilizes long chains of aliphatic compounds to interact with the hydrophobic surface of CNMs and functionalize the surface with active groups. As an example, sodium dodecyl sulfate (SDS) is a well-known anionic surfactant for dispersing CNTs, which can be absorbed to the surface of CNTs and cover them with active sulfate groups[60]. The second method of non-covalent assembly is π - π stacking in which the pyrenyl group is used to interact with CNMs. The pyrenyl group is well known to be highly aromatic in nature and able to bind strongly with the basal plane of graphite and/or sidewalls of the nanotubes via π - π stacking, thus providing a fixation point for the attachment of functional components[61]. The other method is called polymer wrapping in which polymer molecule can be absorbed onto the surface of CNMs and form a coating layer through electrostatic interactions. The functional groups of the polymer enable the assembly of a variety of organic and inorganic nanostructures[62]. Table 1.2 highlights the different

Table 1.2 Overview of different functionalization approaches on CNMs

Functionalization				
Interaction mechanism	Types	Active functional groups	Examples	Potential application
Covalent bonds	Oxidation	-COOH	Ag-CNM,	Composites
	Oxygen plasma	-OH -O-	Au-CNM	
Hydrophobic	Non-ionic aliphatic	-SH, -COOH, -NH ₂	Au-CNM (dodecanethiol), TiO ₂ -CNM (oleic acid)	Photo switch, chemical sensor.
	Ionic aliphatic	Charged group	Ru-CNM(SDS)	Fuel cell
π - π stacking	Non-ionic aromatic	-SH, -COOH, -NH ₂ , -OH	Ag-CNM (benzyl mercaptan), Co-CNM (pyrene derivative)	Conductive material
	Ionic aromatic	Charged group	Pt, Pd, Ru, Rh-CNM (IIL)	Electrochemical catalysis
Wrapping	Homopolymer	Charged group, -NH ₂	Au, Fe ₃ O ₄ -CNM (PSS/PDDA)	Nano-reinforced fiber material
	Copolymer	Charged group, -SH	Au, Cu, Fe-CNM (PSMA)	Single-electron device
	DNA	-SH,	Au-CNM (DNA)	Vapor sensing
Doping		N	Au, Ag, Cu, Pd (N-CNM)	Supercapacitor field emission
Direct deposition	E-beam deposition,		Ag-CNM	Nano electronic device
	Electrochemical deposition		Au, Ag, Cu, Pd-CNM	

functionalization approaches which have been used for assembling various organic and inorganic functional nanostructures onto the surface of CNMs[39].

1.4 Scope and outline

The thesis focuses on developing flexible and scalable chemical approaches to functionalize CNMs and investigating their potential applications. According to the bonding difference between CNMs and the functional components, these functionalization approaches can be divided into two groups, namely covalent functionalization and non-covalent functionalization.

Chapter 1 gives a general introduction of different nanomaterials and their unique properties, especially on CNMs. In addition, different functionalization processes and how they manipulate CNMs structures and properties are described and explored.

Chapter 2 focuses on the covalent functionalization of CNMs. It includes two parts of work that target on CNTs and graphene respectively. The first part introduces an efficient surface activation process to covalently functionalize CNT surface and also a stable metal deposition process to deposit finely grained and uniform silver nanoparticles on CNTs. The fabrication process and characterization of silver coated CNT hybrid nanomaterials are presented and discussed. Mechanisms of surface activation and metal deposition process are also investigated for optimizing the uniformity and packing density of silver nanoparticles on CNT surfaces. These developed processes have the benefit of low costs, simplicity and good compatibility, showing great potential in the mass production of metallic particle supported CNMs. The second part presents the covalent functionalization of graphene based films (GBFs) that act as heat spreaders for hotspot-cooling. The covalent bonding between GBF and the substrate is realized via the linkage of a silane coupling agent which can significantly reduce the thermal interface resistance and improve the cooling effect. Such results show great potential in the thermal management of high-power density devices.

Chapter 3 presents a non-covalent functionalization process for synthesizing intrinsically flexible multi-functionalized CNT based hybrid nanowires. The multi-functionalized CNT based hybrid nanowires were synthesized with different functional materials on the surface of CNTs to produce a metal nanoparticle coating layer and form uniform dispersions whilst possessing the CNT's original structural integrity and high flexibility. The synthesized multi-functionalized CNT based hybrid nanowires possess many excellent properties, such as good dispersability and stability in various polar solvents, large flexibility and high electrical conductivity. These extraordinary properties facilitate the application of hybrid nanowires in the fabrication of flexible and stretchable circuits (FSCs) with high resolution. The electro-mechanical properties and reliability of FSCs are also investigated. The results show good flexibility and stable electrical performance of FSCs under different structural deformation. Light-emitting diodes (LED) demonstrators are also fabricated, which illustrate the superior mechanical and electrical performance of multi-functionalized CNT based FSCs.

The conclusions and future outlook are summarized in chapter 4

Chapter 2

Covalent Functionalization of CNMs

2.1 Covalent assembly of silver coated CNTs hybrids

Covalent assembly of nanostructures onto CNTs surface is based on covalent functionalization of CNT, in which the oxygen-containing groups (e.g carbonyl and carboxyl groups) are introduced directly onto the CNT surfaces through bonding to the π -conjugated skeleton of the CNTs under aggressive conditions, such as strong acid oxidation or plasma etching. The process of surface activation of CNT and silver nanoparticles deposition are schematically illustrated in Figure 2.1. Generally, pristine CNTs have highly inertial surfaces and easy to form agglomerations, which make them difficult to obtain uniform and densely packed silver nanoparticles coating layer on their surfaces. To solve this problem, the surface of CNTs needs to be activated with nucleation sites which would benefit the growth and attachment of silver nanoparticles. In previous reports, the activation process of CNT was usually carried out through the etching using concentrated acids[63], [64]. However, such treatment lack of efficiency on creating sufficient nucleation sites for silver nanoparticle growth and led to a poor coating effect.

Instead of using acid etching, pristine CNTs were treated by a multi-oxidant solution under low-power ultrasonication in this thesis. The multi-oxidant solution consists of both the intercalating agent (H_2SO_4) and oxidant (KMnO_4) which could significantly increase the surface roughness and also functionalize the CNTs with large amounts of oxygen-containing functional groups. After the surface activation, palladium seeds were deposited on the surface of CNTs through the redox reaction between palladium (Pd^{2+}) and Tin (Sn^{2+}) ions. Those seeds would act as catalysts for silver nanoparticles growth in the following process. Finally, the coating of silver nanoparticles on the surface of CNTs was carried out in a complex

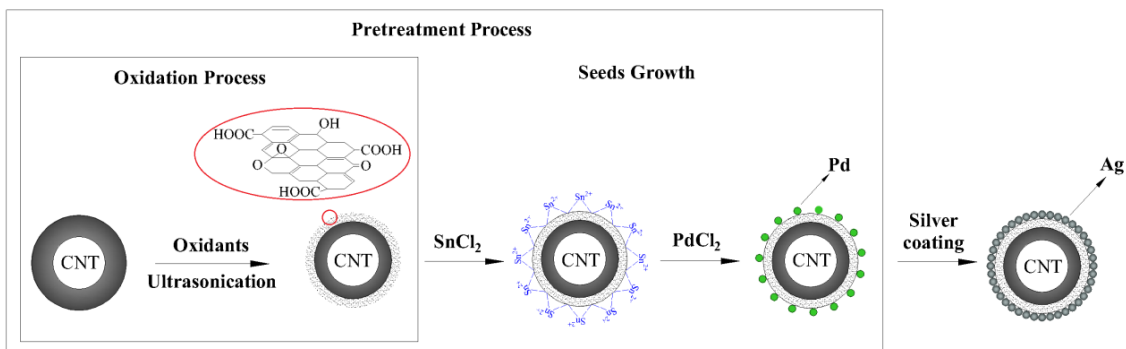


Figure 2.1 Schematic drawing of the CNT surface activation process and silver nanoparticle deposition process. Pristine CNTs were activated by simultaneously oxidation and ultrasonication, and then coated with palladium nano-seeds. The silver nanoparticle deposition on the surface of CNTs was carried out in a complex solution which can maintain a stable deposition speed within a certain period.

solution containing silver ion source ($\text{Ag}(\text{NH}_4)^+$), reducing agent (Co^{2+}) and chelating agent (ethylenediaminetetraacetic acid (EDTA)). During the silver coating process, cobalt (II) ions, acting as the reducing agent, reacted with silver ions to form metallic silver nanoparticles on the surface of the CNTs. Also, due to the chelation of EDTA, the reaction between silver ions and cobalt ions is stable which can benefit for achieving highly uniform and densely packed silver nanoparticles coating layer on CNT surfaces.

2.1.1 Surface activation of CNTs

Pristine CNTs were treated by different activation processes. A Fourier-transform infrared spectroscopy (FTIR) analysis was employed to study the functional group change on CNT surfaces during the activation process and also compare the activation efficiency of different activation processes and characterize the functional groups on CNT surfaces. Four samples were tested and analyzed, including the reference (pristine CNTs), CNTs oxidized by nitric acid at 80°C for 1h (N-CNT), CNTs oxidized by the mixture of nitric acid and sulfuric acid (1:3) at 20°C for 24h (N/S-CNT) and CNTs treated with the multi-oxidant solution of $\text{H}_2\text{SO}_4/\text{KMnO}_4$ under low-power ultrasonication (M-CNT). As shown in Figure 2.2a. From the spectrum, pristine CNTs show some inherent characteristic peaks corresponding to oxygen-containing groups, like epoxy, carbonyl and carboxyl, which could be resulted from the production process used by the material supplier. For the sample of N-CNT, no obvious change of functional groups was detected, implying that the reaction between the nitric acid and CNTs was too much slow. The etching of nitric acid is hard to break the stable sp^2 -carbon structure of CNTs. It has been found that mild reaction conditions would benefit the formation and stability of oxygen-containing groups. Therefore, those peaks on N/S-CNT corresponding to the vibration of C-O and C=O groups became more intensive than that of pristine CNTs. However, such treatments still lack of efficiency for activation of CNT's surfaces due to a long etching time. By comparison, the spectrum of M-CNTs showed significant increases of oxygen-containing groups on CNT surfaces. For example, the characteristic peaks at 1220 cm^{-1} and 1700 cm^{-1} which correspond to the breathing vibration of C-O and the stretching vibration of C=O from carbonyl and carboxyl groups became much more intensive. Some new strong peaks appeared in the range of $1400\sim 1536\text{ cm}^{-1}$, which represented the stretching vibration of C-O. And two more characteristic peaks were formed at the position of 2870 cm^{-1} and 2960 cm^{-1} , corresponding to the stretching vibration of C-H from methene groups. These results indicate a strong interaction between CNT's surface with the combined oxidant system. Moreover, the whole activation process was carried out at a lower temperature ($30\sim 40^\circ\text{C}$) for only 0.5h, which showed a much higher efficiency than that of traditional acid etching processes.

Raman spectroscopy was employed to examine structural changes of CNTs before and after surface activation by multi-oxidants. Figure 2.2b shows the typical spectrum of pristine CNTs which presents a strong G peak at 1575 cm^{-1} indicating the high crystalline CNT's structure and a weak D peak around 1335 cm^{-1} meaning the existence of low defects in the sp^2 network of nanotubes[65]. Compared to that, the intensity of D peak at 1335 cm^{-1} increased significantly after surface activation. This result means that the defect area on the surface of CNTs was greatly expanded due to the treatment of multi-oxidants. Previous

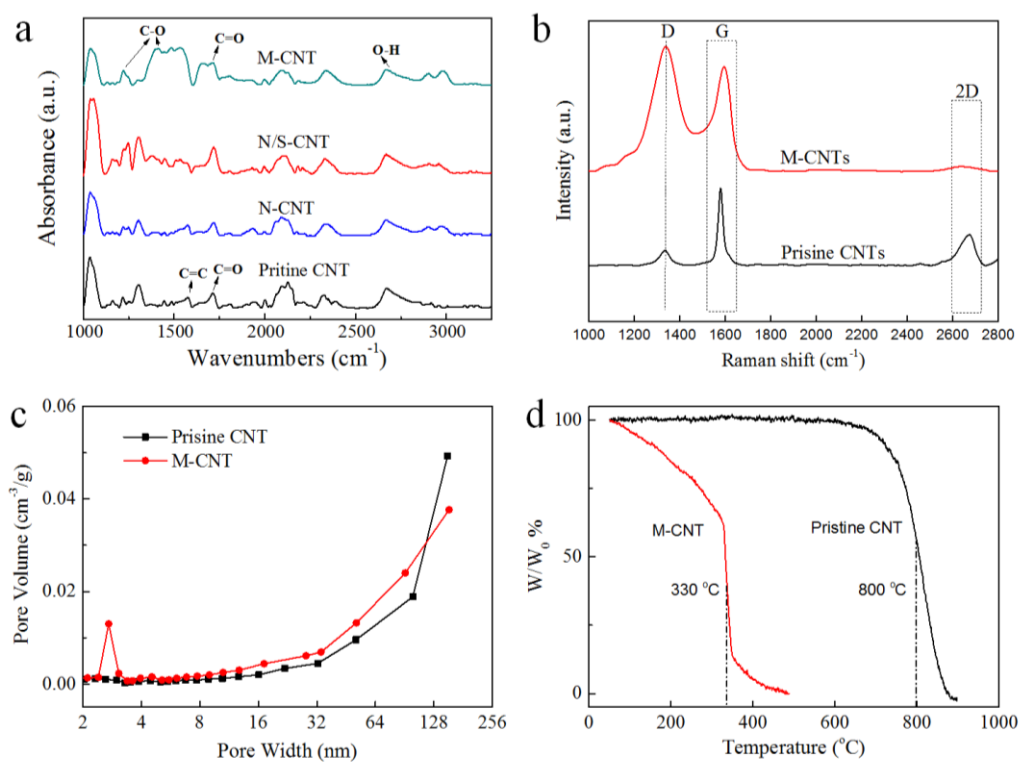


Figure 2.2 (a) FTIR spectra of pristine CNTs, CNTs oxidized by nitric acid at 80 $^{\circ}\text{C}$ for 1h (N-CNT), CNTs oxidized by a mixture of nitric acid and sulfuric acid at 20 $^{\circ}\text{C}$ for 24h (N/S-CNT) and CNTs treated with the multi-oxidant solution under ultrasonication for 0.5h (M-CNT). (b) Raman spectroscopy of pristine CNTs and M-CNTs. (c) Pore volume and distribution of pristine CNTs and M-CNTs. (d) TGA curves of pristine CNTs and M-CNTs.

research has shown that the defects are essential for the targeted growth and attachment of silver nanoparticles on the surface of CNTs. They would act as nucleation sites to trigger the deposition of silver nanoparticles[66]. Therefore, the amount and size distribution of nucleation sites became important for determine silver nanoparticle's uniformity and packaging density on CNT surface. To analyze the average size of those nucleation sites, Barrett-Joyner-Halenda (BJH) pore volume and distribution tests were carried out, and the result was shown in Figure 2.2c. Different from the pristine CNTs, M-CNTs present a strong peak at the position of 3 nm in the pore distribution curves, implying a high size uniformity of the created nucleation sites. Also, the surface area of M-CNTs even doubled from the original value of 16.3 m²/g to 33.5 m²/g according to the analysis of Brunauer-Emmett-Teller (BET), which was attributed to the formation of nano-scaled nucleation sites.

Thermogravimetric analysis (TGA) was employed to investigate the impact of surface modification on the physical property changes of CNT. As shown in Figure 2.2d, two samples, pristine CNTs and M-CNTs, were programmed to heat from 50 °C to 900 °C in dry air atmosphere with a heating rate of 20 °C/min. As a result of burning, there was no residue detected for both two samples, which indicated the high purity of material. Also, it has been found that the decomposition temperature of M-CNTs was decreased from 800 °C to 330°C as compared with pristine CNTs. This is due to the defects and oxygen-containing groups generated on CNTs surface during the activation. Specifically, the decomposition of activated CNTs started from the reaction of oxygen-containing groups with their adjacent carbon atoms, which caused a gradual weight loss at lower temperature. Further increase of temperature would lead to a growth of the contact surface and higher reactivity between CNT and oxygen. As a result, a complete reaction between CNTs and oxygen took place at 330°C. The decrease of decomposition temperature also identified the structural changes of M-CNT, which showed consistency with Raman analysis.

A transmission electron microscopy (TEM) study was carried out to understand the morphology and lattice changes of M-CNTs. Figure 2.3a shows the structure of pristine CNTs. As seen, pristine CNTs used in this work have an average diameter of 100 nm which is larger than the conventional CNTs. The reason for choosing such a large-sized CNT as the initial material is to achieve higher silver nanoparticle packaging density on the surface of each individual CNT. Due to the size limitation, smaller CNTs (< 10 nm) can only be surrounded with one or two nanoparticles (3 nm), which is hard to meet the requirement[66]. Besides a large diameter, Figure 2.3b presents a highly oriented structure comprising of numerous parallel graphitic layers, indicating the high crystallinity of pristine CNTs. Compared to that, some obvious morphology changes were noticed after surface activation of CNTs. As seen from Figure 2.3c, the cross-section view of M-CNTs shows a strong contrast between the weak outer-layer and strong inner layers, and the outer layer has an average thickness of 10 nm. This phenomenon was caused by the intercalation and oxidation effects of the oxidants which changed the lattice structure in the surface layer. As shown in Figure 2.3d, the lattice structure close to surface area was partly disrupted and became small debris with random orientations, which was different from the highly oriented inner graphitic layers. Moreover, the distance between the adjacent graphitic layers was also expanded from original 0.3 Å to 0.6 Å due to the insertion of oxygen-containing groups.

The activation mechanism of the multi-oxidant solution was investigated and illustrated in

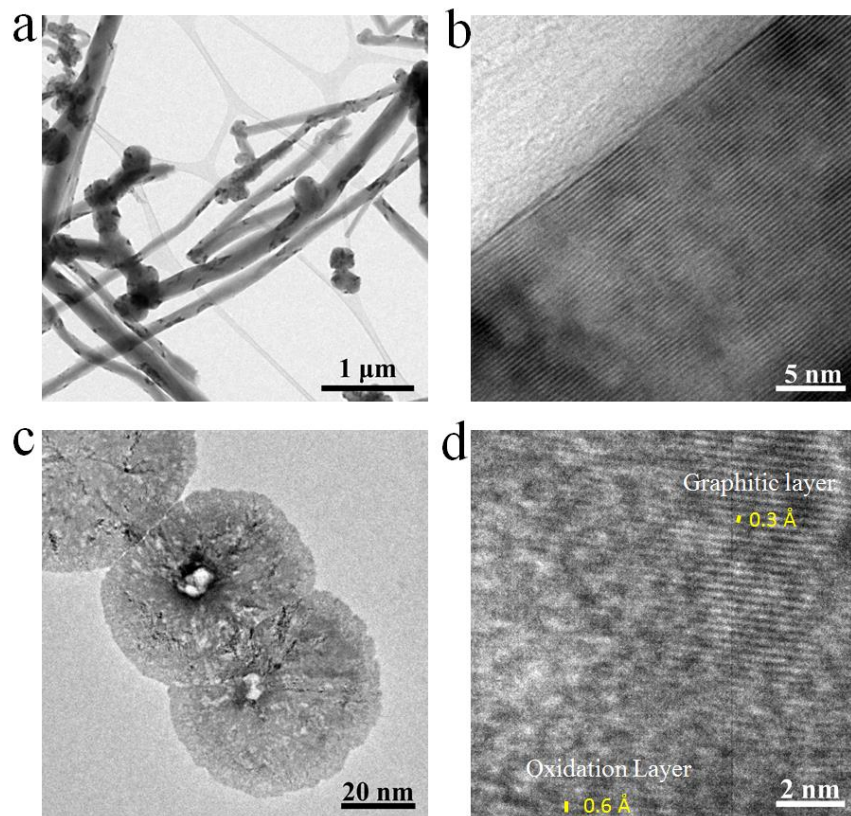


Figure 2.3 (a,b) TEM images of pristine CNTs with different magnifications. (c) TEM cross-section view of CNTs activated by the multi-oxidant solution (M-CNT). (d) TEM image of the structural change of M-CNTs on graphitic lattice after oxidation.

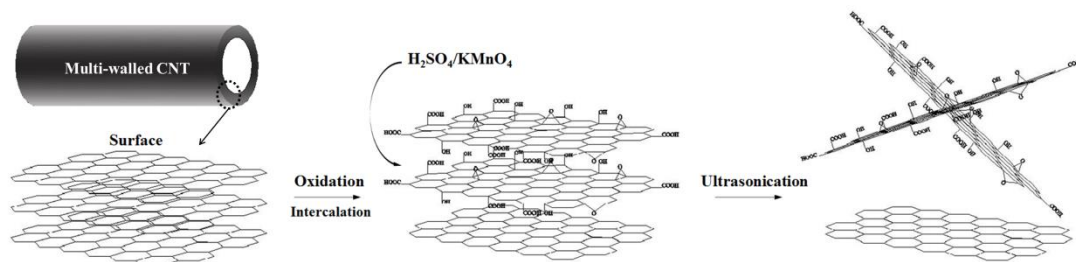


Figure 2.4 The activation mechanism of CNT surface by the treatment of simultaneously oxidation and ultrasonication.

Figure 2.4. As shown, the oxidation process usually started from the edge and surface defect areas of CNTs. Those positions are more vulnerable under the attack of oxidant molecules due to their incomplete sp^2 carbon structure. Consequently, many oxygen-containing groups were generated at those places, such as phenolic, ether, carboxyl and carbonyl groups. With the expansion of defect area, sulfuric acid, as the intercalating agent, started to penetrate into the inner graphitic layers of CNTs and caused further oxidation[67]. This would weaken the Van der Waals' force between adjacent graphitic layers and lead to the expansion of layer distance. Besides the chemical oxidation treatment, low-power ultrasonication was also maintained during the whole activation process to increase surface roughness of CNTs and improve the activation efficiency. Due to the treatment of low-power ultrasonication, large amount of nano-scaled cracks and holes were generated at the surface of CNTs, which would act as nucleation sites for silver nanoparticles growth. In addition, the activation degree of CNTs could be regulated through controlling the reaction time and temperature to meet different requirements.

2.1.2 Deposition of silver nanoparticles on the activated CNTs

The coating of silver nanoparticles on the surface of CNTs was carried out in a complex silver plating solution where mild reaction conditions were maintained to refine nanoparticle's size and geometry. Figure 2.5a shows the morphology change of CNTs after silver coating. As seen, large amount of nanoparticles was uniformly deposited around the whole CNT's surface and formed a densely packed layer. The mean diameter of the nanoparticles is about 3 nm as shown in Figure 2.5b. No free particles or obvious agglomerations were detected. The high uniformity of nanoparticle's diameter and distribution was attributed to the activated surface of CNTs which restricted the size of individual particles and prevent their agglomerations. X-ray diffraction (XRD) study was employed on CNT samples at different stages to identify the elementary composition of the coating layer. As shown in Figure 2.5c, pristine CNTs exhibited a typical graphitic XRD pattern. The strongest diffraction peak appeared at 25.5° can be indexed as the (002) reflection of the hexagonal graphitic structure. The other two peaks located at 43° and 53° are also associated with (100) and (004) diffractions of graphite respectively[68]. However, after surface activation, the sharpness of the peak at the angle of 25.5° showed a significant decrease. Meanwhile, the other graphitic peaks shifted towards lower angles. The change of the graphitic XRD pattern means that the graphitic structure of

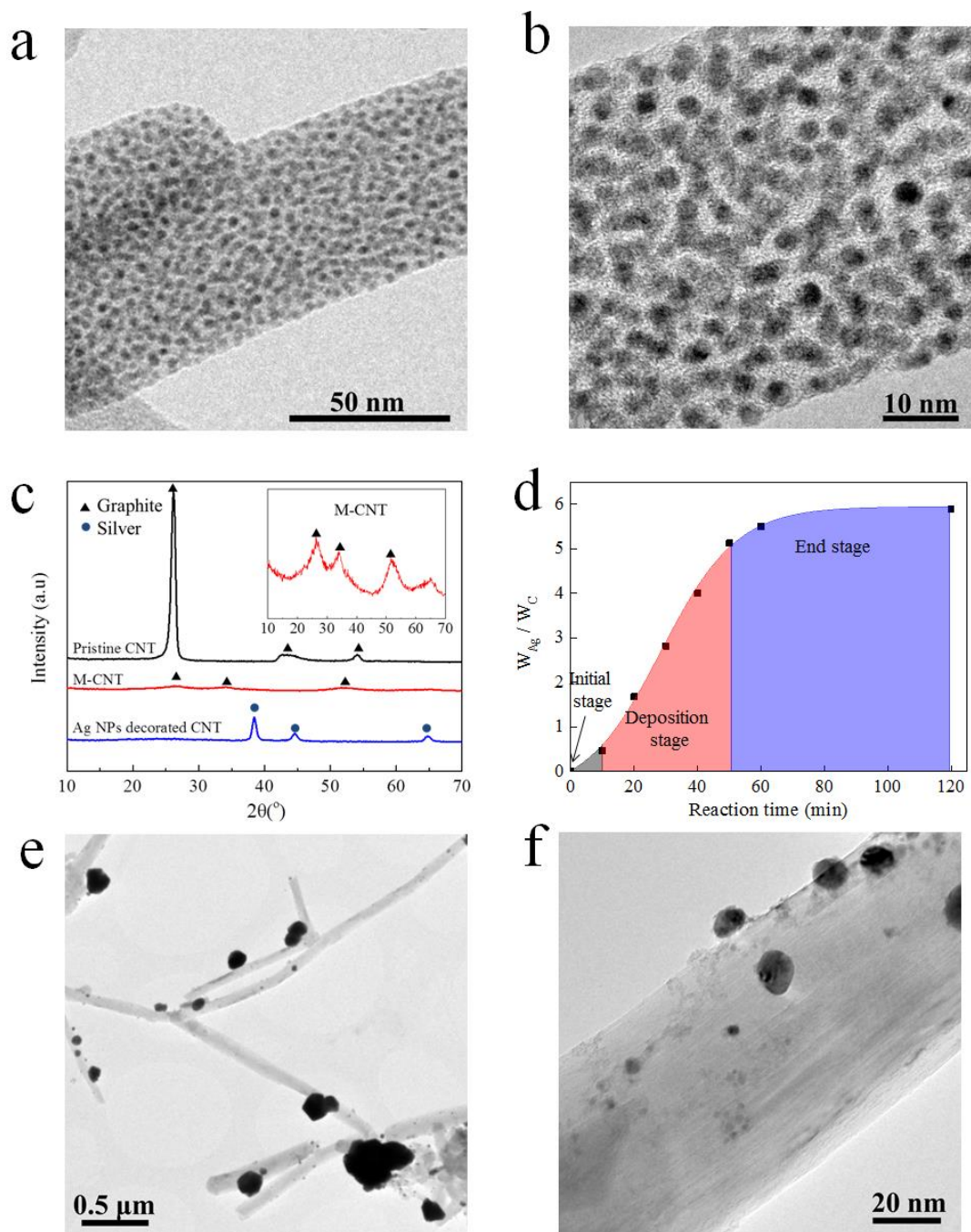


Figure 2.5 (a,b) TEM images of silver nanoparticles decorated CNTs with different magnifications. (c) X-ray diffraction (XRD) patterns of pristine CNTs, activated CNTs, and silver nanoparticles decorated CNTs. (d) the change of silver weight ratios deposited on the surface of CNTs as a function of the reaction time measuring by TGA. (e,f) TEM images of silver coated N/S-CNTs. CNTs were activated by a mixture of nitric acid and sulfuric acid (1:3) at 20°C for 24h, and glucose was used as the reducing agent for silver nanoparticle deposition.

CNTs was modified during the surface activation process. This result is also corresponding to the disappearance of graphitic peaks after silver coating on CNT. Besides that, there are three new intensive peaks that appeared at the angle of 37.9 °, 44.1 °, and 64.8 ° after silver coating. They are indexed as (111), (200) and (220) reflections of silver's face-centered cubic (FCC) structure respectively, implying the presence of silver with high crystallinity[69].

To understand the reaction mechanism of the silver plating process and precisely control the size and deposition density of silver nanoparticles, systematic study of the silver deposition speed was performed by TGA. Different CNT samples with varied silver plating time were collected and burnt completely in a flowing dry air to record the change of silver mass ratios expressed as W_{Ag}/W_C . W_C represents the weight of CNTs. Figure 2.5d shows the change of silver mass ratio as a function of plating time. According to silver growth curve, there was a short initial stage lasting for 10 min at the beginning of silver coating process. During this stage, the silver deposition speed was relatively slow. Possible reasons could be that most of silver and cobalt ions were encapsulated by the chelating agents and formed stable compounds respectively. The reaction speed at this stage was mainly dominated by the slow spreading and decomposition process of metal ion chelates. After the initial stage, reactions between silver ions and cobalt ions became much more active due to palladium's catalytic action. As a result, large amount of silver nanoparticles were generated and deposited onto the surface of CNTs. The deposition stage continued about 40 min with the silver mass ratio increased from 0.5 to 5. Importantly, a stable deposition rate was exhibited during this stage due to the slowly decomposition processes of the chelated compounds. It would avoid a rapid growth of silver nanoparticles and benefit for obtaining a uniform deposition layer. The plating rate then reached a plateau with 60 minutes and diminished completed after prolonged plating due to the depletion of reactants in the plating bath. According to the calculation of silver input-output ratio, the reacted silver had reached up to 70% in the solution while the reduction of the rest 30% became difficult because of the prevention of chelating agents. Further prolongation of reaction time would not increase the silver mass ratio, indicating that silver nanoparticles deposition had been accomplished.

Similar experiment with N/S-CNTs (HNO_3/H_2SO_4 , 20°C, 24h) and glucose as the reducing agent was also performed to compare silver coating effect with the result in this work. As shown in Figure 2.5e-f, the surface of CNTs was only decorated by very limited amount of silver nanoparticles. Also, silver nanoparticles showed irregular shapes and different sizes ranging from 10 nm to 200 nm. Such a poor silver coating result could be caused by insufficient nucleation sites for silver nanoparticles growth and attachment. Meanwhile, the formation of large particles was a result of rapid growth of silver nanoparticles due to the fast reaction between silver ions and glucose. These results indicated the importance of an efficient activation process and a stable silver deposition speed to the uniformity of nanoparticles coating layer. Besides using conventional glucose for reduction, previous reported plating methods employing e.g. sodium borohydride or dimethylamine borane species as reducing agents unavoidably lead to the generation of hydrogen gas during plating process[70], [71]. It may take over the nucleation sites for the growth of silver nanoparticles and interfere in the morphology and coverage of silver nanoparticles, which would also lead to a poor silver coating effect. These results show advantages of both our surface activation and silver coating processes on realizing high uniformity and large

packaging density of silver nanoparticles at the surface of CNTs.

2.2 Covalent functionalization of GBF for improving its cooling property.

2.2.1 Graphene for hotspot cooling

Integration and power density of microelectronic systems have been continuously increasing for decades. Efficient systematic thermal management solutions are an immediate requirement to dissipate the large amount of heat generated by the integrated chips and devices. Aiming for high thermal conductive, cost-effective and eco-friendly processes, intensive efforts have been put into the research of novel thermal management materials in both academia and industry during recent years. Among all the alternatives, graphene is one of the most inspiring materials that may provide potential solutions to these technological barriers. Composed of one or few atomic layers of sp^2 -bound hexagonal carbon lattice, phonon transfer inside graphene becomes extremely efficient, which lead to an outstanding in-plane thermal conductivity of about 5800 W/mK. Consequently, different approaches of utilizing graphene for heat dissipation have been investigated and reported in literature. For example, single-layer graphene sheets fabricated from chemical vapor deposition was transferred onto the top surface of hotspots and acted as heat spreader which showed certain decrease of the working temperature on active devices[72]. However, this approach has some limitations including low transfer efficiency, complexity and relatively high costs. Graphene/polymer composites have also been fabricated and utilized for thermal management[73]. However, the thermal conductivity values of the composites are very limited due to the large phonon boundary scattering of individual graphene sheets.

Instead of using single layer graphene or graphene/polymer composites, a special free-standing GBF is developed for thermal management of power devices in the current thesis work. The GBF is composed of horizontally aligned reduced graphene sheets made by chemical exfoliation. This aligned microstructure can offer the film with many advantages, including good flexibility, strong mechanical strength, and particularly, high in-plane thermal conductivity. The extraordinary mechanical and thermal properties of the GBF facilitate it as the heat spreader to dissipate heat in the x-y direction. In addition, a small functional molecule is employed to increase the bonding between GBF and substrates surfaces to minimize the thermal interface resistance and improve the cooling performance of the film.

2.2.2 Fabrication of GBFs

Free-standing GBFs are fabricated through self-assembling and reduction processes of graphene oxide (GO). As a derivative of graphene, GO is prepared through the chemical oxidation and exfoliation of graphite flakes. As a result, it contains large amount of oxygen functional groups mainly located at the edge of graphene domains, including hydroxide groups, carboxyl groups and epoxy groups. The presence of oxygen functional groups make

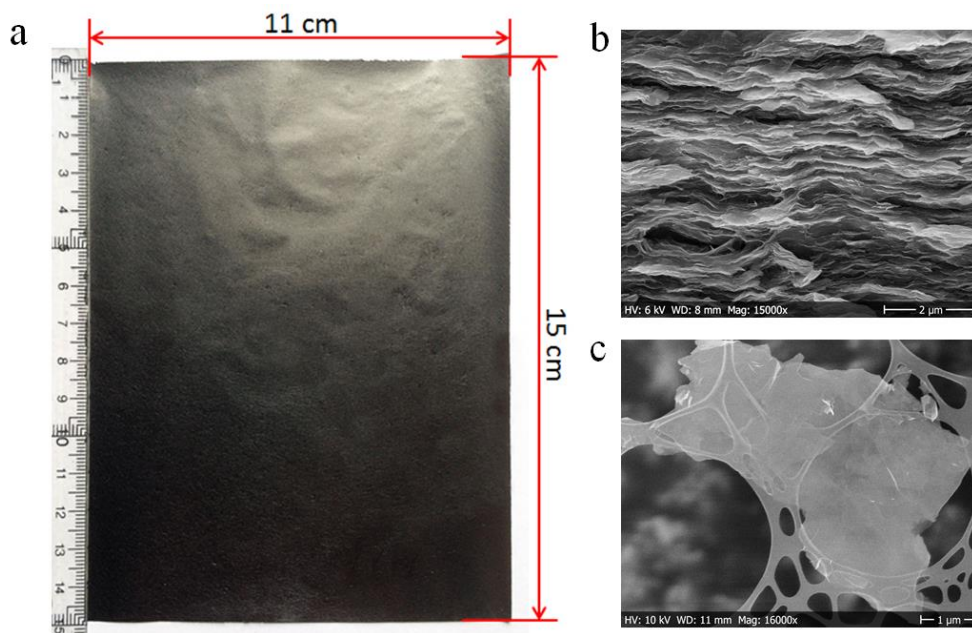


Figure 2.6 (a) Smooth and free-standing GBF fabricated through self-assembling of graphene sheets. The size of the GBF is about 11×15 cm, and the thickness of the film is 20 μm. (b) SEM cross-section view of GBF. The self-assembled, free-standing GBF exhibited a highly aligned, layered structure. (c) SEM image of an individual GO sheet. The as-prepared GO sheet has a large lateral size which is about 10μm.

GO sheets to be strong hydrophilic and can form homogeneous colloidal suspensions in aqueous medium due to the hydrogen bonds with water molecules. Particularly, the homogeneous GO aqueous dispersion can induce a transition from the isotropic to liquid-crystalline phase upon a high filler content, which would lead to the self-assembly of various bulk materials, such as particles, fibers and films[74]. It has been found that the liquid-crystalline property of GO is directly related to the aspect ratio of the filler particles and the concentration of the suspension. GO can be considered as an amphiphilic molecule because it consists of different hydrophilic (oxygen functional groups) and hydrophobic parts (graphene domains). At a very-low concentration of GO with a high content of water (< 1 mg/mL), the GO dispersion can become totally random without any order. However, upon an increase in the concentration, the GO sheets exhibit a high affinity to minimize the free energy of the system through the alignment of the hydrophobic parts by π - π stacking, which can form a self-assembled structure. It has been reported that GO suspension with a large filler lateral size (> 5μm) and high concentration (> 2 mg/mL) is desirable to assemble highly oriented anisotropic GBFs. Therefore, GO sheets are fabricated by following a modified Hummer's method in the absence of a sonication step. Figure 2.6c shows the SEM image of the prepared GO sheet which has an average size of 10 μm. The obtained GO sheets are dispersed into a certain amount of water to form a homogeneous suspension with a concentration of 5 mg/mL by gentle shaking. The size of GO sheet and the concentration of the suspension have been proved to be sufficient enough for inducing the self-assembling of GBF under low temperature heating. The prepared GO suspension is de-bubbled under vacuum with a pressure of 10 mpa for 0.5 h to completely remove the dissolved air, and then casted on a glass substrate for drying at 50 °C. After 24 h, a thin film comprising of aligned

GO sheets can be obtained. The reduction of GO film is carried out in a water bath containing L-ascorbic acid which acts as the reducing agent. The reduction temperature is kept at 95°C and the time is about 2 hours. After reduction, the GBF film together with the glass substrate is taken out from the water bath and rinsed for three times by deionized water, and then dried at room temperature for overnight. The final free-standing GBF can be obtained after peeling off the film from the glass substrate. Figure 2.6a shows the morphology of the prepared GBF. It shows a smooth surface with a large dimension of 11 × 15 cm. The thickness of the GBF is regulated around 20 μm through controlling the volume of the suspension. The large size and uniform structure of prepared GBF show the great potential of the self-assembling process on fabrication of high quality films in large-scale. Figure 2.6b shows the cross-section view of the GBF. It can be found that the self-assembled, free-standing GBF exhibited a highly aligned, layered structure which gives rise to much-enhanced physical and mechanical properties. In particular, the maximum in-plane thermal conductivity of the self-assembled GBF reaches to 1642 W/mK according to the measurement of the laser flash technique (Netzsch LFA 447). This result is superior to most of the commercial graphite films which only have a thermal conductivity of 100~800 W/mK. Possible reasons could be that the graphene sheets in GBFs have much more tight and oriented alignment than that of commercial graphite films which are fabricated through compressing the graphite flakes under high pressure.

2.2.3 Functionalization of GBFs for improving its cooling performance

The extraordinary thermal and mechanical properties show great potentials of GBFs as heat spreader for cooling power devices. However, there are still some challenges that could limit its heat dissipating performance during the realistic application, including a poor thermal coupling between free-standing GBF and device surfaces and high thermal contact resistance caused by mismatching of surfaces and roughness. In order to address these challenges, the surface of the GBF which contacts with device surfaces is functionalized with a silane coupling agent. As a small molecule, the silane coupling agent could both react with the

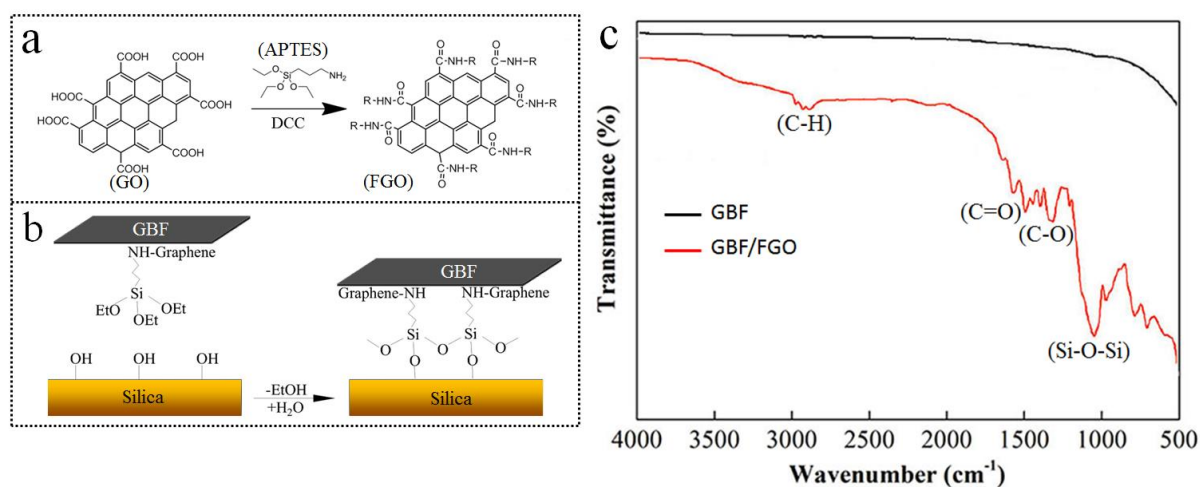


Figure 2.7 (a) Schematic of functionalization of GO with APTES molecules. (b) Schematic of bonding GBF with silica surface by using FGO. (c) FTIR spectrum of pure GBF and GBF with spin-coated FGO.

oxygen functional groups located at the plane and the edge of graphene sheets, and also form covalent bonds with silicon dioxide or metal oxide surfaces. As a result, molecular bridges could be built between the GBFs and the device substrates, and thus improve the heat transfer efficiency from the power devices.

Figure 2.7a-b show the schematics of preparing functionalized GO (FGO) and the bonding mechanism of GBF on the silica substrate surface. The preparation of FGO is realized via the condensation reaction of the carboxyl groups of GO and the amino groups of (3-Aminopropyl)triethoxysilane (APTES) under the catalyst of dicyclohexylcarbodiimide (DCC). The reaction would result in the formation of covalent bonds between GO and APTES and further functionalized GO with active silane groups. Therefore, FGO, as the binding material between GBF and the silica substrate, can be considered as an amphiphilic molecule which consists of hydrophilic parts (silane groups) and hydrophobic parts (graphene domains). The silane groups of FGO can cross-link with each other, and also react with the amorphous silica layer of the substrate to build covalent silicon-oxygen bonds whilst the graphene domains of FGO can bind strongly with the surface of GBFs via π - π stacking. FTIR studies are also conducted to examine the functional group changes on the GBF before and after spin coating of FGO (GBF/FGO). As shown in Figure 2.7c, there are no significant characteristic peaks for oxygen groups in the spectrum of pure GBF sample, indicating the complete reduction of oxygen functional groups. After spin-coating of FGO, the characteristic peaks of C=O and C-O at the position of 1725 cm^{-1} and 1300 cm^{-1} represent the oxygen functional groups of GO. In addition, a new characteristic peak corresponding to stretching of C-H groups from the APTES molecules is observed at the position of 2929 cm^{-1} . More peaks are found at the position of 1034 cm^{-1} and 691 cm^{-1} and represent the vibrations of Si-O-Si and Si-C of APTES. These results indicate the successful functionalization of GBF with FGO.

A thermal testing platform is designed to characterize the heat dissipating properties of functionalized GBF. To simulate the heat generation process of power devices, micro platinum (Pt)-based resistors are employed as the hotspot which can cause a significant temperature increase within one spot. The assembly of GBF onto the surface of the testing platform is realized through a self-developed tape assisting transfer process. GBF with square shape ($1 \times 1\text{ cm}$) is firstly transferred onto a thermal release tape and then spin-coated with a thin layer of FGO (10~20 nm). After that, the functionalized GBF is transferred onto the thermal testing platform through releasing the thermal release tape by heating. In addition, a copper (Cu) heat sink is fixed on the top of GBF by mechanical springs to further dissipate the heat to the atmosphere. The usage of Cu heat sink allows the test platform to be operated at a high power density without failure.

The surface temperature distribution, peak and average temperature of the thermal testing platform are examined by infrared imaging (IR) camera. The operating currents for all the testing platforms are the same (120 mA) to maintain a constant heat generation speed. To ensure the same light emissivity from the substrate, the bottom surfaces of all the thermal testing platforms are also coated with graphite. IR images are taken when the testing platform reaches to the thermal steady state to minimize the deviations. The results are shown in Figure 2.8. As seen, the peak temperatures of bare platform, platform with GBF and platform with functionalized GBF are $121.9\text{ }^\circ\text{C}$, $115.2\text{ }^\circ\text{C}$ and $110.9\text{ }^\circ\text{C}$ respectively, and the average temperatures of each testing platform are $97.2\text{ }^\circ\text{C}$, $93.8\text{ }^\circ\text{C}$ and $91\text{ }^\circ\text{C}$. It can be found that the

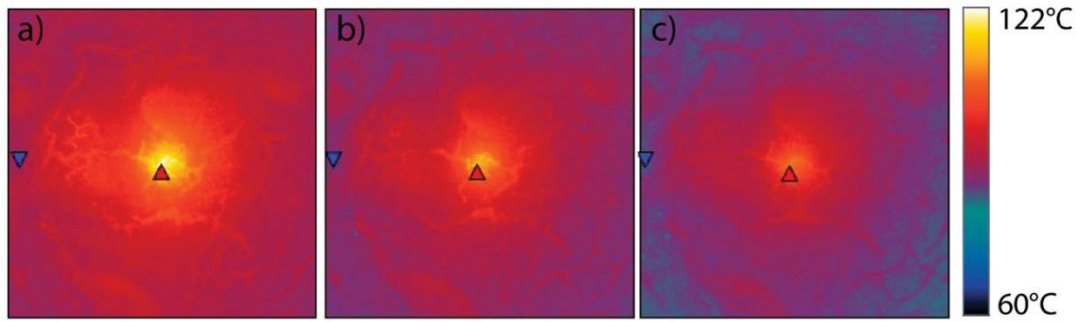


Figure 2.8 IR images of (a) the bare platform, (b) platform with GBF and (c) platform with functionalized GBF. The peak temperatures for each platform are 121.9 °C, 115.2 °C and 110.9 °C respectively, and the average temperatures of each testing platform are 97.2 °C, 93.8 °C and 91 °C.

peak temperature of the platform with functionalized GBF decreased more than 11°C than the bare platform and 5°C than that of pure GBF, indicating the efficient heat dissipation of functionalized GBF. These results show the great potential of using functionalized GBF as heat spreader for managing the thermal issues in power devices.

Chapter 3

Non-covalent Functionalization of CNMs

3.1 Multi-functionalized CNT based hybrid nanowires

Non-covalent functionalization processes utilize various functional molecules or active species as assembly mediators to functionalize the surface of CNMs via non-covalent interactions such as hydrophobic, π - π stacking, and wrapping interaction. The assembled mediators would then act as binding points for anchoring other molecules or nanomaterials. Different from the covalent functionalization processes, the great advantage of non-covalent functionalization processes is to protect CNTs structure and properties from destruction. Therefore, there is a growing interest on development of non-covalent assembly processes. Here, a new surface modification process for synthesizing intrinsically flexible multi-functionalized CNT based hybrid nanowires is presented. The key benefit of the hybrid nanowire lies in their high electrical conductivity and flexible structures to maintain stable electrical and mechanical performances under significant structural deformation. The fabrication processes of multi-functionalized CNT based hybrid nanowires are schematically illustrated in Figure 3.1. The surface of CNTs was successively wrapped with firstly a cross-linkable (3-aminopropyl)triethoxysilane (APTES) layer, then a silica layer, followed by palladium nanoparticle and silver nanoparticle deposition. Every functional material in a hybrid nanowire has been specifically chosen for its beneficial properties: CNTs act as a flexible framework as well as additional electron pathways. APTES improves the dispersion of CNTs in polar solvents through bringing in hydrophilic silane and amino groups on the surface of CNTs. The mesoporous silica layer is used as templates for the attachment and

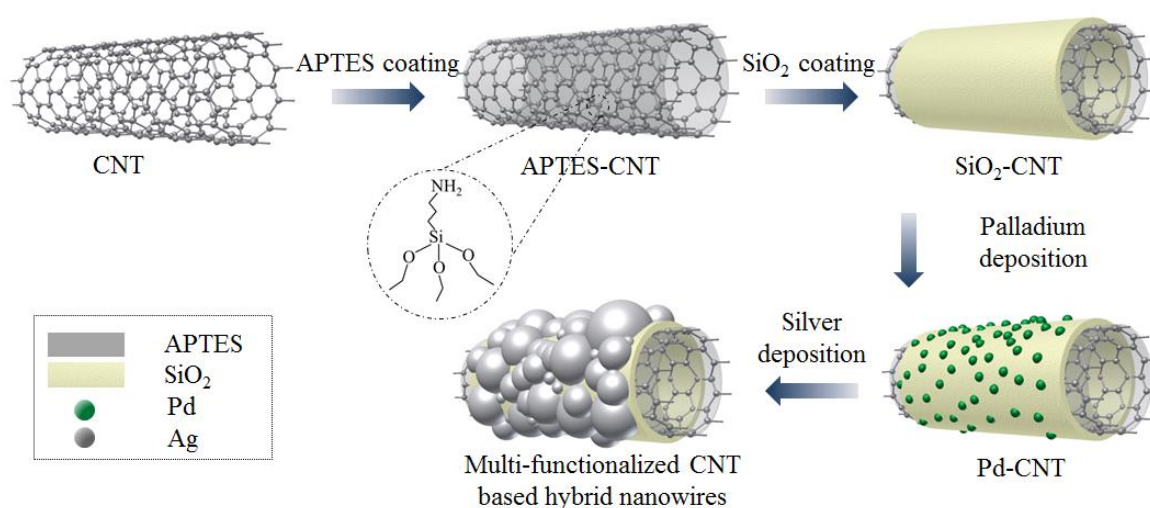


Figure 3.1: Schematic of the various modification steps in the synthesis of multi-functionalized CNT based hybrid nanowires. The surface of CNTs was coated with APTES, silica, palladium nanoparticles and silver nanoparticles.

deposition of metallic nanoparticles. Palladium nanoparticles served as catalysts to provide nucleation sites for silver growth. Finally, silver nanoparticles are the main conductive media to improve the contact surface of the hybrid nanowires and build high-efficiency conductive networks.

3.1.1 Functionalization of CNT surface by APTES and SiO₂

Pristine CNTs have very large aspect ratios and highly inactive surfaces, which make them uneasy to form homogeneous and stable dispersion. To address such a challenge, the required surface activation of CNTs needs to be carried out. In previous reports, this was generally achieved through an oxidation pretreatment of CNTs or surfactant assisted separation processes[75], [76]. However, such treatments always lead to severe structural damage as well as poor electrical and mechanical performance to CNTs. In this work, CNTs were coated with a cross-linked APTES polymer layer (APTES-CNTs). The large amounts of hydrophilic groups of APTES, such as Si-OH and -NH₂, would assist CNTs to be homogeneously dispersed in polar solvents. Importantly, the APTES layer can be completely removed in the follow-up process without having any adverse effects on the CNT's properties. The reaction mechanism of forming APTES-CNTs is schematically illustrated in Figure 3.2a. CNTs exhibit a negatively charged surface in ethanol at high pH value (pH > 7), which can attract the positively charged APTES monomer through electrostatic absorption[77]. The attracted APTES monomers cross linked with each other under alkaline conditions and formed a coating layer on the surface of CNT. Figure 3.2b shows the difference of the CNT dispersions

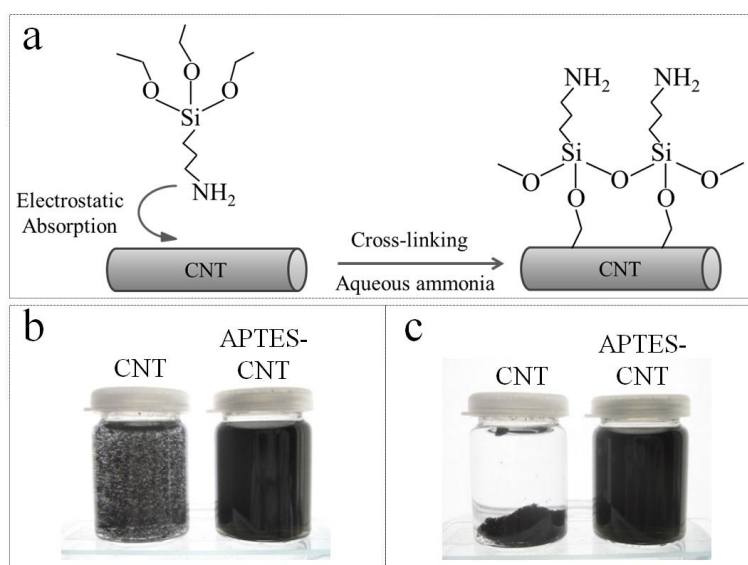


Figure 3.2: (a) The reaction mechanism of forming APTES layer on CNT surface. Positively charged APTES monomer could be attracted by the negatively charged CNTs through electrostatic absorption. Crosslinking of APTES monomers would take place under alkali condition, and an APTES coating layer can be formed at the surface of CNTs. (b) Dispersion of CNTs in ethanol before and after APTES coating. A homogeneous CNTs ethanol solution was obtained after modification with APTES. (c) Solution stability of CNTs in ethanol without and with APTES coating for the period of one month after preparation. No delamination or sediment was detected in the ethanol dispersion of APTES-CNTs.

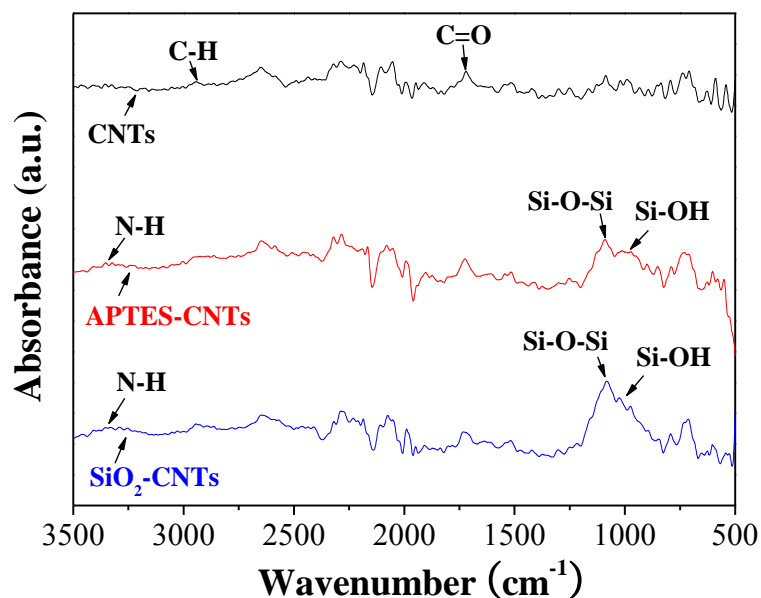


Figure 3.3: FTIR analysis of pure CNT, APTES-CNT and SiO₂-CNT. Compared to the FTIR spectrum of pure CNT, APTES-CNT shows the Si-OH stretching and asymmetric Si-O-Si stretching peaks at 980 cm⁻¹ and 1080cm⁻¹ respectively, and also the N-H stretching peak between 3400-3500cm⁻¹. After silica coating, the peak corresponding to Si-O-Si stretching becomes more intense in the spectrum of SiO₂-CNT. These results indicate the successfully coating of APTES and silica layer.

in ethanol before and after APTES coating. A homogeneous CNT ethanol solution was obtained after functionalizing with APTES. Additionally, the APTES-CNT suspension exhibits good stability for the period of one month after preparation (Figure 3.2c). No sediments were detected in the ethanol dispersion of APTES-CNTs, which indicates the effectiveness of the APTES coating onto the CNT surfaces.

After being functionalized with APTES, silica coating was carried out onto the surface of the CNTs (SiO₂-CNTs) through the hydrolysis reaction of tetraethyl orthosilicate (TEOS) under alkaline conditions to act as templates for metal nanoparticles deposition[78]. FTIR was employed to confirm both the attachment of APTES and formation of SiO₂ around the composite (Figure 3.3). The peaks at 1700 cm⁻¹ and 2900 cm⁻¹ corresponding to C=O and C-H groups indicate that the CNT has defects due to the production processes used by the CNT supplier. After functionalizing with APTES, the peaks corresponding to Si-OH stretching and asymmetric Si-O-Si stretching appeared at 980 cm⁻¹ and 1080cm⁻¹ respectively. Moreover, a broad band located between 3400-3500cm⁻¹ represents N-H stretching of the amino group in APTES. After TEOS treatment, the peak corresponding to Si-O-Si stretching becomes stronger due to the formation of a silica layer.

Transmission electron microscopy (TEM) study was carried out to understand the morphology changes of CNTs before and after the silica coating process. The image of pure CNTs shown in Figure 3.4a indicates a smooth surface with a diameter of 10 nm. In comparison, a shell structure along the axial direction of the nanotubes can be observed from Figure 3.4b, which indicates a successful silica coating on the CNT. The thickness of the silica shell was found to be about 10 nm which can be varied through changing the concentration of TEOS. The impact of the APTES layer to the silica coating was also

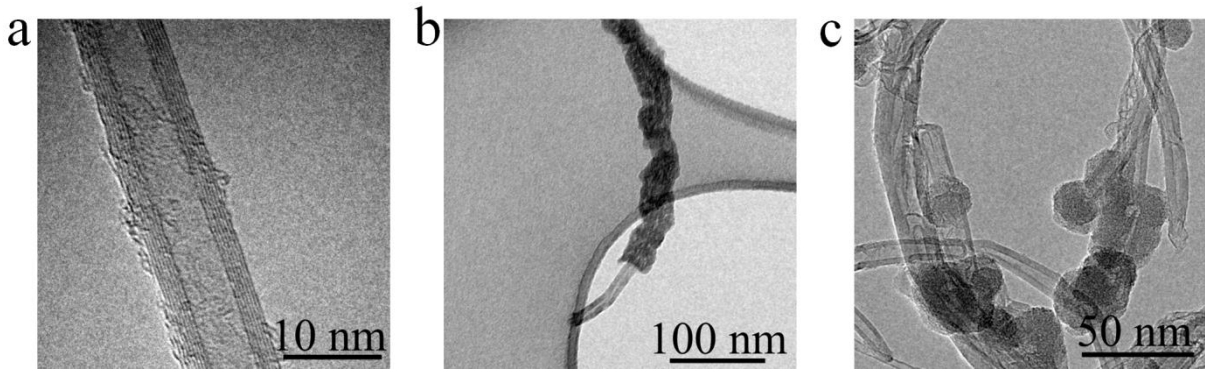


Figure 3.4: (a) A pure CNT with a diameter of 10nm. (b) SiO₂-CNTs. An amorphous silica layer with a thickness about 10nm was deposited at the surface of APTES-CNTs. (c) Control experiment of silica coating directly on CNTs without APTES modification. A random and unselective SiO₂ deposition on CNTs with huge bundles was observed.

examined via a control experiment of coating the silica directly on CNTs without APTES modification layers. It has been found that the deposition of SiO₂ was random and individual CNTs tended to form big bundles (Figure 3.4c). Therefore, it can be inferred that APTES layers were not only assisting the dispersion of CNTs, but also acting as an adhesion layer for the silica coating process.

3.1.2 Deposition of silver nanoparticles on the functionalized CNTs

The SiO₂ layer exhibits a strong binding ability with positively charged ions due to the attraction of Si-OH group, and also a mesoporous structure which would facilitates the targeted metal nanoparticle growth[79], [80]. Figure 3.5 illustrates the deposition of palladium nanoparticles on CNT (Pd-CNTs). Metallic palladium (Pd) nanoparticles were generated through the reduction of Pd²⁺ ions by Sn²⁺ ions which were pre-trapped in the silica layer.

TEM image in Figure 3.6a shows the morphology change of CNT after palladium deposition. A large quantity of Pd nanoparticles with an average particle size of 3nm was uniformly deposited in the SiO₂ layer. Those Pd nanoparticles would act as nucleation sites for the proceeding silver growth on CNTs. Finally, multi-functionalized CNT based hybrid nanowires were obtained through electroless silver plating. Mild reaction conditions were maintained during silver nanoparticle growth to ensure the uniform and complete silver deposition on the CNTs. The degree of silver nanoparticles coverage on the CNT surfaces was found to be very critical for optimizing the electrical performance of the hybrid nanowires. Hence, a series of multi-functionalized CNT specimens were prepared with increased silver

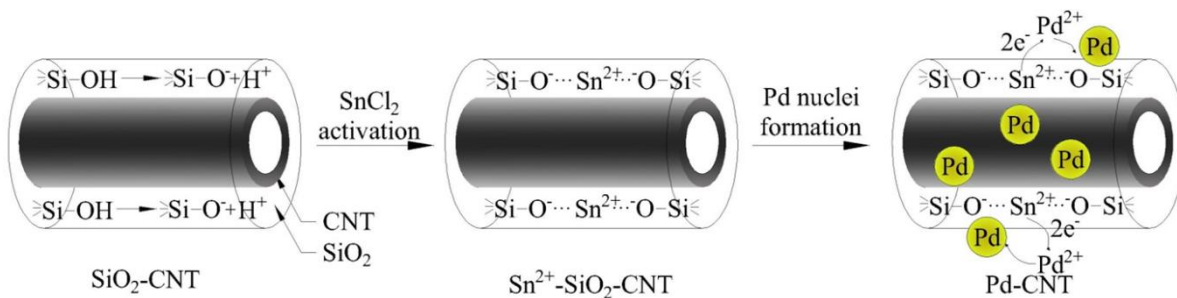


Figure 3.5: Reaction mechanism of palladium nanoparticles deposition in silica layer.

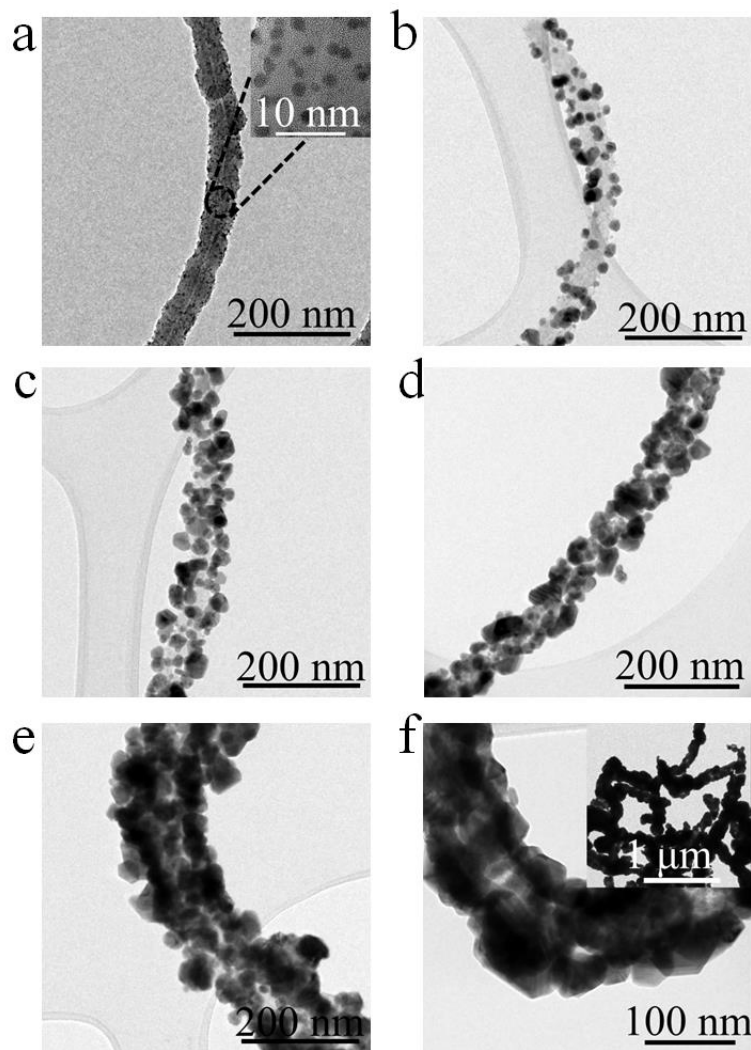


Figure 3.6 (a) Pd-CNTs. Dense and uniform palladium nuclei were deposited in silica layer and no free particle were observed. The inset shows that the average size of palladium nuclei is about 3nm. (b-f) Multi-functionalized CNT based hybrid nanowires prepared with different silver nitrate concentrations. b: 1 g/L; c: 2 g/L; d: 5 g/L; e: 10 g/L; f: 15g/L, the inset shows the zoom out image of hybrid nanowire connection.

nitrate concentrations from 1 g/L to 15 g/L to study the effect of silver nitrate concentration on the metallic coverage of the CNTs. TEM observation shows that the morphologies of the CNTs changed as the silver nitrate concentrations were varied (Figure 3.6b-f). When a lower silver nitrate concentration (1 g/L) was used, small silver nanoparticles with an average size of 20 nm were formed due to presence of inadequate silver precursor sources (Figure 3.6b). Upon increasing the concentration of silver nitrate from 1 g/L to 10 g/L, the average size of silver nanoparticles was increased from 20 nm to 50 nm with an enlarged surface coverage (Figure 3.6c-e). When the silver nitrate concentration reaches to 15 g/L (Figure 3.6f), a layer of densely packed silver nanoparticles was formed around the whole CNTs surface. No free silver nanoparticles or obvious agglomerations were detected after using a higher silver nitrate concentration.

Figure 3.7 shows the XRD patterns for pristine CNTs and the multi-functionalized CNT hybrid nanowires respectively. Peaks located at 38.2° , 44.4° and 64.5° in the sample of multi-functionalized CNT hybrid nanowires are referred to the (111), (200) and (220) planes of the fcc structure of metallic silver, and also the diffraction peak at 26.5° is referred to (002) of graphite. The XRD pattern of Ag-CNTs hybrid nanowires indicates that the silver nanoparticles deposited over the CNT surface have a highly pure crystallinity. These results show advantages of our process on both protecting CNT's structure and coating complete metallic nanoparticle layers compared with the previous reports[81]–[83].

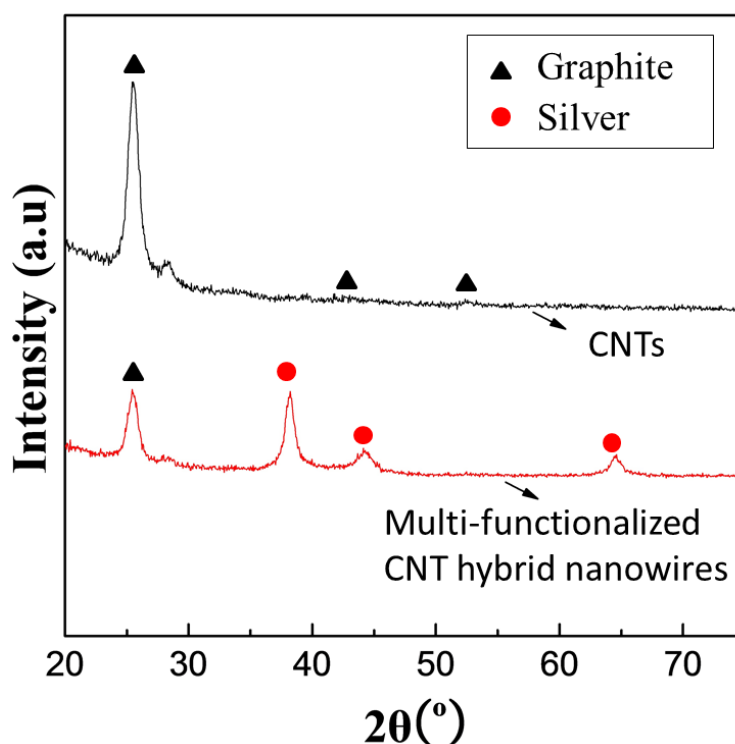


Figure 3.7 XRD patterns for pristine CNTs and the multi-functionalized CNT hybrid nanowires respectively. Peaks located at 38.2° , 44.4° and 64.5° in the sample of multi-functionalized CNT hybrid nanowires are referred to the (111), (200) and (220) planes of the fcc structure of metallic silver, and also the diffraction peak at 26.5° is referred to (002) of graphite.

3.2 Fabrication of flexible and stretchable electrical circuits

3.2.1 Flexible and stretchable circuits

As the demands of modern electronic systems call for increasing functionality, smaller system size, higher device connectivity, better user experience, and all at lower cost, flexible and stretchable circuits (FSCs) are becoming a high-growth technology in the area of electrical interconnects. This is due to their compact nature and high electrical-connection density over the traditional rigid printed circuit boards[84]. Comprising of a deformable substrate and conductive traces, FSCs possess an excellent deformation ability that will facilitate many new applications in the field of portable and wearable electronics, such as paper-like displays[85], smart clothing[86], stretchable solar cells[87], camera eyes[88] and biomedical sensors[89]. However, although the merits of FSCs are significant, there are some challenges that urgently need to be solved. One of the most critical points of this technology is the electro-mechanical reliability of the elastic interconnections, which are challenged in particular by relatively high and complex mechanical loading, such as, bending, compression and elongation[90].

Restricted by the demands of FSCs for high electro-mechanical performance, solutions to address the above problem are very challenging. Traditional strategies have been to use electroplated sinuous metallic wires deposited on deformable polymers, which had demonstrated high electrical conductivity under large tensile strains[91], [92]. However, due to the lack of protection, the metallic wires usually suffer severe structural damage under repeated stretching/releasing cycles, which led to a poor reliability of FSCs and even complete failure. The recent development of patterning techniques has introduced alternative strategies for directly making FSCs patterns with a variety of highly conductive nanomaterials[93], [94]. K. Kordás reported that elastic patterns of carbon nanotubes on a plastic film obtained a resistance of $R_s = 4 \times 10^4 \Omega/\square$ (resistivity of $4 \times 10^4 \Omega \cdot \mu\text{m}$)[95]. J. Wu fabricated a graphene electrode with a peak electrical performance of $R_s = 800 \Omega/\square$ (resistivity of $5.6 \Omega \cdot \mu\text{m}$)[96]. L. Hu achieved a minimum resistance of $R_s = 50 \Omega/\square$ (resistivity of $2 \times 10^2 \Omega \cdot \mu\text{m}$) with a transparent and flexible silver nanowire based electrodes[97]. However, some challenges raised from the material themselves still limit their applications; carbon based nanomaterials, like pristine carbon nanotubes (CNTs) and graphene, can easily form agglomerations that are hard to disperse. This makes it difficult to form uniform patterns, and their relatively high contact resistance to metals might also lead to the poor electrical performance of FSCs. Metal nanowires lack flexibility and suffer structural damage at large strain that can cause the complete failure of FSCs. To satisfy the requirements for developing FSCs with stable electro-mechanical properties and high reliability, it is therefore desirable to synthesize hybrid nanomaterials that possess the high conductivity of metals together with good flexibility and dispersability.

3.2.2 Patterning and fabrication of high-resolution FSCs

Owing to the presence of abundant hydrophilic groups, such as Si-OH and $-\text{NH}_2$, the as-fabricated multi-functionalized CNT based hybrid nanowires were found to be easily

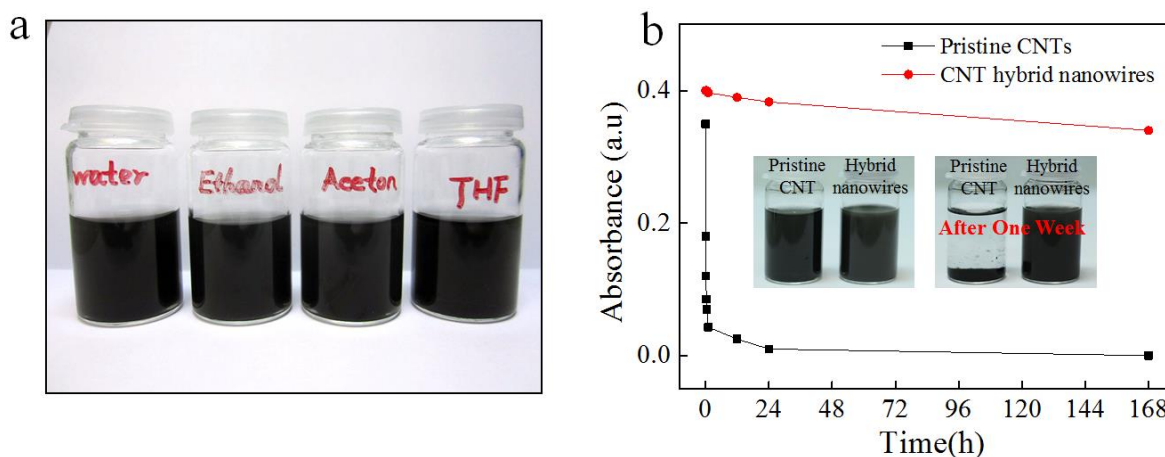


Figure 3.8: (a) Multi-functionalized CNT hybrid nanowires homogeneous dispersions in water, ethanol, acetone and tetrahydrofuran (THF) solvents. Due to the existence of hydrophilic APTES layer, the as-fabricated multi-functionalized CNT hybrid nanowires show good dispersability in various polar solvents with a concentration of 7mg/mL and form uniform suspension. (b) Time-resolved UV-Visible absorbance intensities of pristine CNTs and CNT hybrid nanowires ethanol dispersions at the wavelength of 500 nm. The two dispersions have the same concentration of 0.2 mg/mL and dispersed with ultrasonication before the test. The hybrid nanowire ethanol dispersion showed higher initial absorbance intensity than that of pure CNTs in ethanol, indicating a good dispersion quality of the hybrid nanowires. Moreover, the absorbance intensity of pure CNTs had a significant decrease after 1 h and disappeared after 1 week, representing the delamination of the dispersion. As a comparison, the hybrid nanowire dispersion showed relatively stable UV-Visible absorbance intensities during one week, which indicated the good stability of the hybrid nanowire dispersion. The inset images show the stability comparison of pristine CNTs and CNT hybrid nanowires ethanol dispersions (7 mg/mL) for one week.

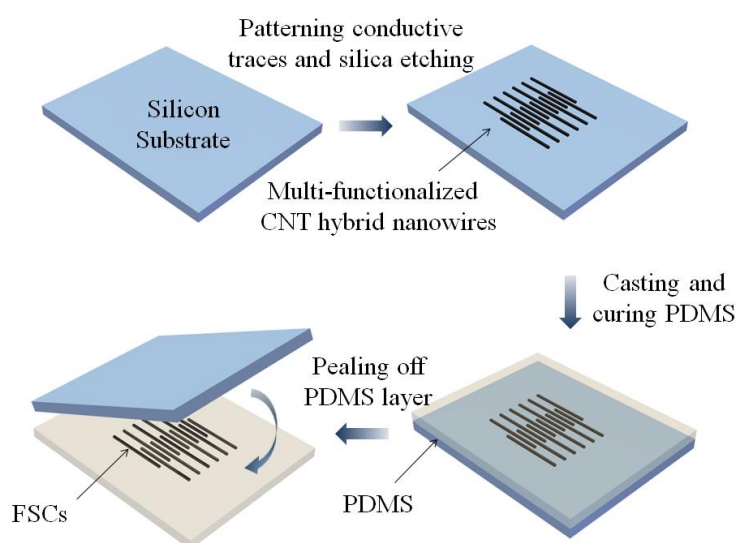


Figure 3.9: Schematic of the preparation of FSCs based on the hybrid nanowires and PDMS.

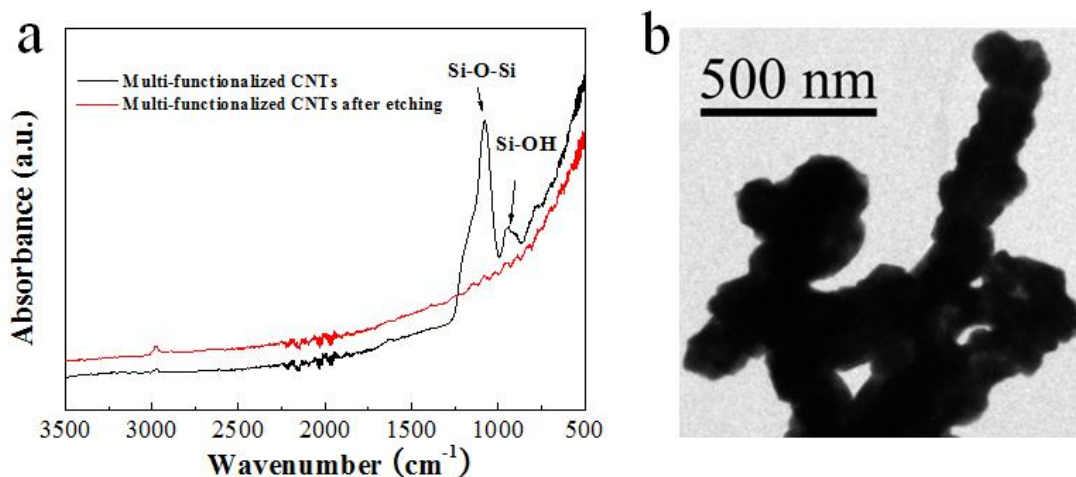


Figure 3.10 (a) FTIR analysis of multi-functionalized CNT hybrid nanowires before and after HF etching. Two characteristic peaks at 1000 cm^{-1} corresponding to Si-O-Si and Si-OH groups disappeared after HF etching of the multi-functionalized CNT hybrid nanowires, which identified the complete removal of silica layer, and also, no other characteristic peaks were found after HF etching indicates that the surface modification process and the HF etching process had no effect to the structure of CNTs. (b) TEM image of CNT based hybrid nanowires after HF etching. It can be seen that the hybrid nanowires still retain a complete silver nanoparticle coating layer after removing both the silica and APTES layer by HF etching.

dispersed in various polar solvents and form homogenous suspensions (Figure 3.8a). Ultra violet-Visible (UV-Vis) spectroscopy analysis further shows that the hybrid nanowire ethanol dispersions have good uniformity and stability (Figure 3.8b). These results made it possible to fabricate FSCs with uniform structures via direct patterning processes.

A mask patterning process was developed and utilized for FSCs fabrication, which is schematically illustrated in Figure 3.9. The prepared hybrid nanowire ethanol dispersion were filtrated and deposited onto silicon substrates through patterning of a shadow silicon mask. After removing the mask, the deposited structure on the substrate was then washed with a diluted hydrofluoric acid (HF) solution and dried in air to both completely remove all forms of silica (both APTES and silica layers) and restore the flexibility & conductivity of multi-functionalized CNT based hybrid nanowires.

FTIR analysis were carried out for multi-functionalized CNT samples before and after HF etching, results were shown in Figure 3.10a. Two characteristic peaks at 1000 cm^{-1} corresponding to Si-O-Si and Si-OH groups disappeared after HF etching of the multi-functionalized CNT based hybrid nanowires, which identified the complete removal of the silica layer. Moreover, no other characteristic peaks were found after HF etching indicates that the surface modification process and the HF etching process had no effect to the structure of CNTs. Figure 3.10b shows the TEM image of CNT based hybrid nanowires after HF etching. It has been found that the hybrid nanowires still retain a complete silver nanoparticle coating layer after removing both the silica and APTES layer by HF etching. PDMS was then cast onto the top of the silicon substrate and infiltrated through the gap in the patterned structures to provide mechanical support. After curing, the PDMS layer was peeled off from the substrate. The conductive traces were embedded below the PDMS surface to form

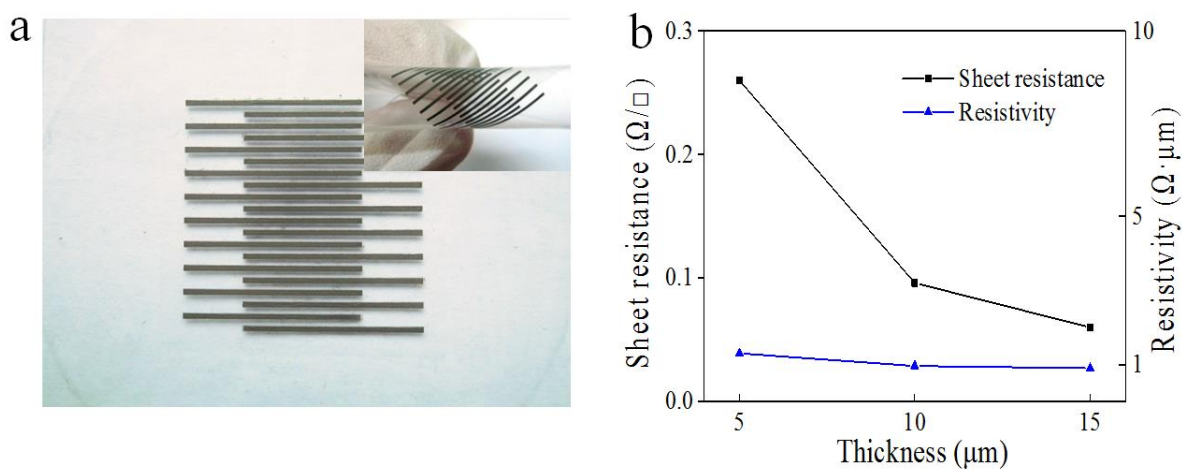


Figure 3.11: (a) FSCs with 10/10 lines, each line has a length of 1.5 cm and a width of 500 μm. The insets show the optical images of bent (180°). (b) Sheet resistance and resistivity change as a function of the hybrid nanowire conductive layer's thickness. The FSCs showed a stable initial resistivity value under a small variation of thicknesses (5 μm), indicating the good interconnection of individual hybrid nanowires at around 10 μm.

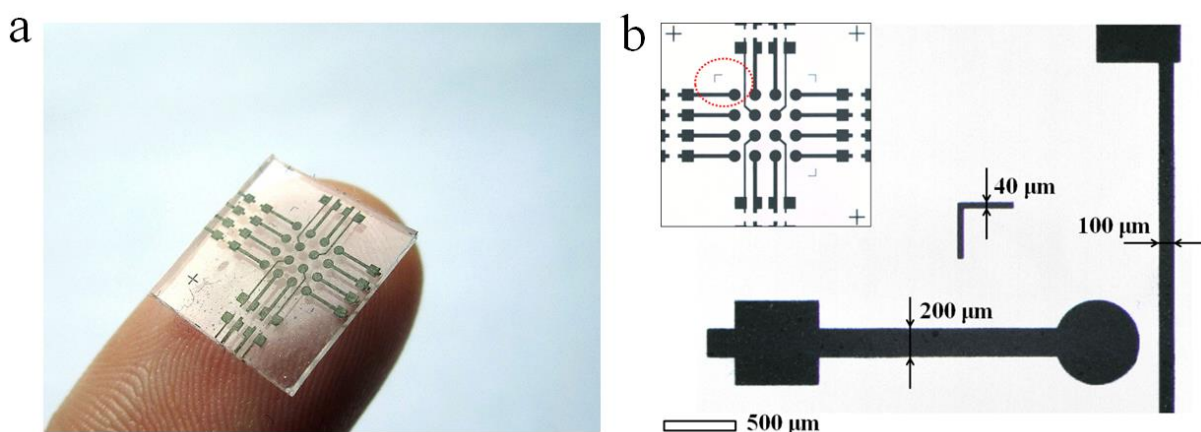


Figure 3.12 (a-b) Optical image of FSCs (8*8mm) with a different pattern, which indicates the ability of multi-functionalized CNT hybrid nanowires for making arbitrary and fine patterns. Each unit of FSCs consists of line structures with varied widths, and the minimum width demonstrated in the unit is 40 μm. The thickness of the pattern is about 10 μm. Two-probe test of this smaller FSC shows the same resistivity result as the conductive traces with a diameter of 500 μm, indicating the capability of the hybrid nanowires for making different patterns.

conductive FSCs. Figure 3.11a shows parallel patterns of a 20-wire array with each wire having a length of 15 mm and a width of 500 μ m. The effect of thickness variation to the resistivity change was also studied. As shown in Figure 3.11b, different conductive traces with different thicknesses ranging from 5 μ m to 15 μ m were fabricated, and their respective resistivity and sheet resistance were plotted by the four-probe method. The resistivity was found to be almost constant in this range, which indicates good interconnection of the individual hybrid nanowires. Therefore, the thickness of patterned conductive traces was regulated around 10 μ m through controlling the volume of the solution to give stable electro-mechanical properties and ensuring the good reliability of the FSCs. In the following discussion, sheet resistance for 10 μ m thick traces will be used as the main electrical performance indicator. The average thickness of PDMS substrate is 500 μ m. The inset in Figure 3.11a shows FSCs at the bending state. It can be seen that the conductive line remains both continuous and uniform when rolled up till 180°, with no indication of breakage or voids. Figure 3.12a shows another example of FSCs with different patterns. Each unit of FSCs consists of line structures with varied widths, and the minimum width demonstrated in the unit is 40 μ m (Figure 3.12b). It shows the potential ability of multi-functionalized CNT based hybrid nanowires for fine patterning.

3.3 Electro-mechanical properties and reliability of FSCs

3.3.1 Electrical resistivity change of FSCs as a function of silver coverage ratios

The degree of silver nanoparticle coverage on CNT surfaces plays a crucial factor in the electrical performance of FSCs. To study this effect, different FSPC samples were prepared by using multi-functionalized CNT based hybrid nanowires with varied degrees of silver coverage ($C_{AgNO_3} = 0 \sim 15$ g/L). The sheet resistance of each sample was tested by the four-probe method, and results were shown in Figure 3.13. It has been found that the sheet resistance of FSCs decrease rapidly with increasing silver nitrate concentrations, compared to the reference sample made from pure CNTs (1316 Ω/\square , resistivity of $1.3 \times 10^4 \Omega \cdot \mu\text{m}$). For samples prepared with silver nitrate concentrations of 1 g/L, 2 g/L, 5 g/L and 10 g/L, the sheet resistance values are 100.81 Ω/\square , 4.07 Ω/\square , 0.38 Ω/\square and 0.15 Ω/\square respectively and the percolation threshold for an exponential decrease in resistance was located at 2g/L. It indicates that silver nanoparticles at the CNT surface were interconnecting and provide the main contribution to electrical conductivity when the silver nitrate concentration reached 2 g/L. The minimum sheet resistance (0.096 Ω/\square , resistivity of 0.96 $\Omega \cdot \mu\text{m}$) was reached when CNTs were fully covered with silver nanoparticles ($C_{AgNO_3} = 15$ g/L), which means that a complete silver nanoparticle coating layer can minimize the contact resistance and provide sufficient conductive channels inside the conductive traces. These results are consistent with the morphology change of multi-functionalized CNT based hybrid nanowires as observed in Figure 3.6b-f. Moreover, high temperature annealing can further decrease the sheet resistance of the conductive traces due to the sintering of silver nanoparticles. However, a rigid silver

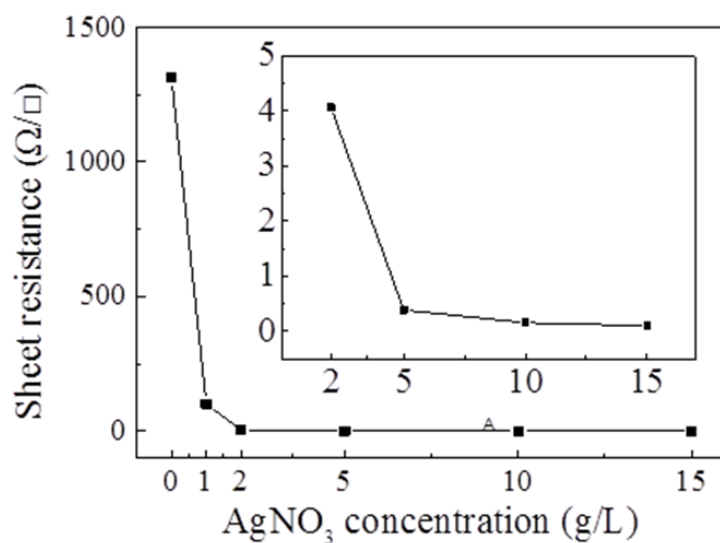


Figure 3.13 Electrical tests show a decrease of sheet resistance with the increase of silver nanoparticles coverage on CNT. A minimum resistance of $0.096 \Omega/\square$ (equivalent resistivity of $0.96 \Omega \cdot \mu\text{m}$) at 0% strain was obtained when CNT was totally covered by silver.

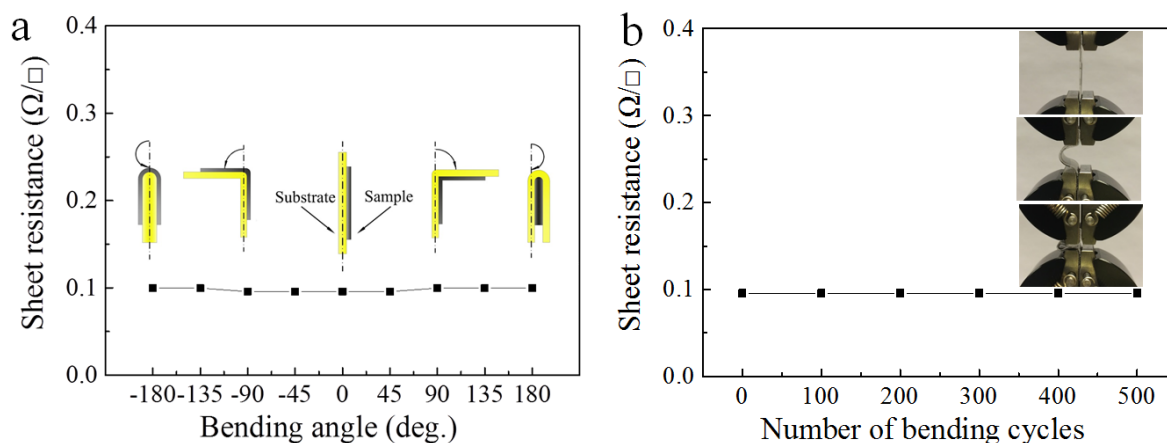


Figure 3.14: (a) The sheet resistance change of FSCs ($C_{\text{AgNO}_3}=15\text{g/L}$) as a function of bending angle. A small variation of sheet resistance less than 3.8% was observed when FSCs were bent up to 180° , which indicated the stable electro-mechanical properties of FSCs. (b) Resistance results of FSCs upon bending cycles. FSCs demonstrate a high reliability after 500 cycles of bending/releasing.

shell can hinder the flexibility of the hybrid nanowires, which would lead to a poor electro-mechanical performance under large structural deformation.

3.3.2 Flexibility and reliability of FSCs

The bending effect on the sheet resistance of FSCs comprising of multi-functionalized CNT based hybrid nanowires ($C_{AgNO_3} = 15\text{g/L}$) was investigated further on a high precision load/displacement measurement machine with a strain rate of 5 mm/s. Figure 3.14a shows the sheet resistance variation of FSCs as a function of bending angles ($-180^\circ \sim 180^\circ$). Notably, a small variation of resistance less than 3.8% was observed when the sample was bent up to 180° , and it recovered after straightening. Notably, after 500 cycles for a bending angle of 180° , the electrical resistance remained constant, as shown in Figure 3.14b. These results show the excellent electro-mechanical stability of hybrid nanowires during bending tests compared with conventional materials used in flexible electronics, even graphene which shows a resistance increase of 20% after the third bending cycle due to the crack formation[98].

The microstructural analysis of the FSCs further helps to understand the reasons for their outstanding electrical performance. As shown in Figure 3.15a, the hybrid nanowires entangled with each other to form a conductive network after patterning and acted as the main electron pathways for FSCs. Figure 3.15b shows the surface morphology of FSCs after PDMS infiltration. It can be seen that PDMS has penetrated through the conductive layer and filled all along the inside gaps of the conductive network. The complete filling of PDMS provides enough mechanical support for absorbing stresses and protecting the multi-functionalized CNT based hybrid nanowires from structural damages under large deformation.

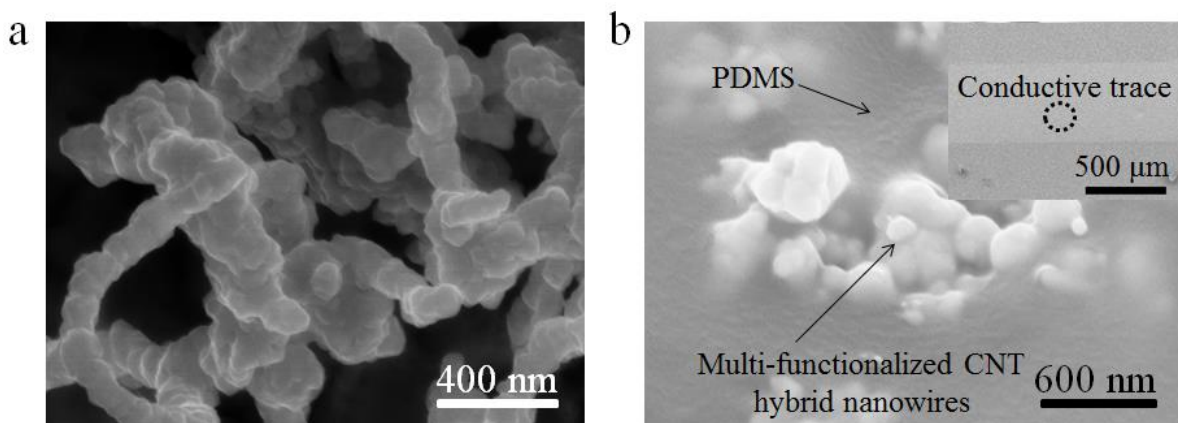


Figure 3.15 (a) SEM image of the hybrid nanowires after patterning. The hybrid nanowires were entangled with each other to form a conductive network. (b) SEM images of FSCs after PDMS infiltration. The multi-functionalized CNT hybrid nanowires are protected by PDMS through embedding into the PDMS layer. Due to the penetration of PDMS into the conductive traces, the internal space inside the conductive traces was fully occupied by PDMS which could provide as mechanical support for individual hybrid nanowire during large structure deformation. It would make the FSCs to be more reliable than the ordinary plated metal traces on PDMS substrate. The inset image shows the image of FSCs. The average diameter of each conductive trace is 500 μm .

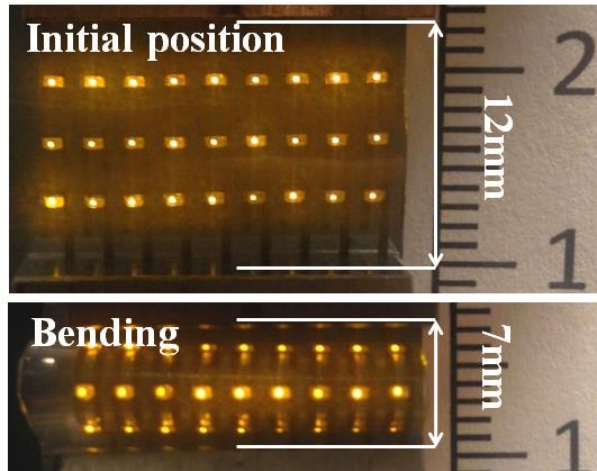


Figure 3.16: Optical images of LED array integrated at FSCs with and without bending. LEDs remained lit with the same illumination intensity as at 0% strain when the demonstrator was bent to 180°. It indicates the stable electrical performance of the FSCs.

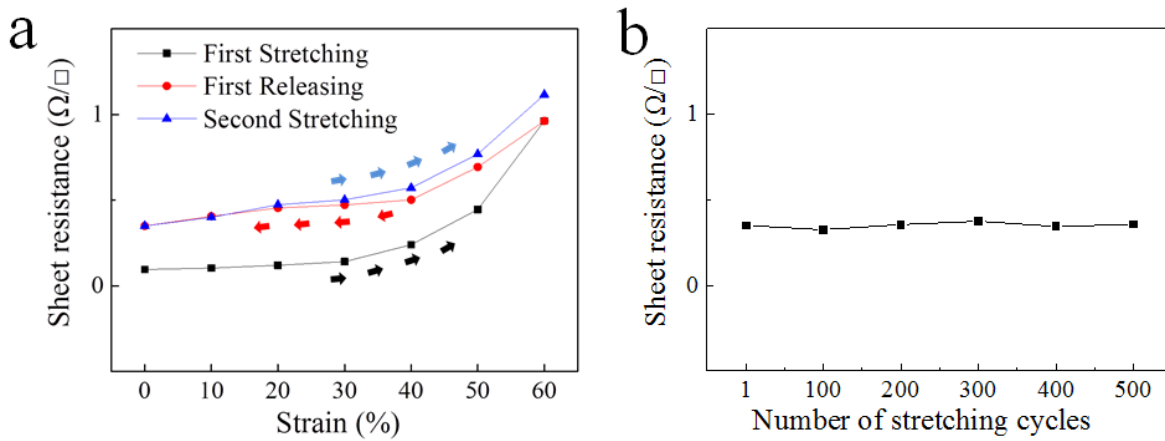


Figure 3.17 (a) Resistance change of FSCs ($\text{CAgNO}_3=15\text{g/L}$) as a function of applied strains. The resistance remained stable ($\sim 0.1 \Omega/\square$) under 30% stretching. Further increasing the tensile strain to 60%, the resistance showed an increase from $0.1 \Omega/\square$ to $0.96 \Omega/\square$. Upon the release of the strain, the sheet resistance was partially recovered and stabilized at $0.35 \Omega/\square$ with 0% strain. (b) Reliability of FSCs under repeated stretching/releasing cycles. After the first stretching/releasing cycle, FSCs showed a stable sheet resistance ($0.35 \Omega/\square$ at 0% strain) with less than 8% variation after 500 repeated cycles.

To demonstrate the electrical resistance change of FSCs during bending, an array of LEDs was assembled on the top of the parallel wires and sealed with PDMS layer. Figure 3.16 shows the lit image of LEDs before and during bending. It was found that LED demonstrators showed the same illumination intensity at the bending state as the initial state, which indicates the stable electrical performance of FSCs. This result was also consistent with the bending test (Figure 3.14a).

3.3.3 Stretchability and reliability of FSCs

The electrical performance of FSCs ($C_{\text{AgNO}_3} = 15 \text{ g/L}$) was also investigated as a function of tensile strain on the high precision load/displacement measurement machine at the same strain rate of 5 mm/s. Figure 3.17a shows the results at a maximum strain of 60%. During the first stretching/releasing cycle, the resistance remained stable ($\sim 0.1 \text{ } \Omega/\square$) under 30% stretching. Further increasing the tensile strain to 60%, the resistance showed an obvious increase from $0.1 \text{ } \Omega/\square$ to $0.96 \text{ } \Omega/\square$. Upon the release of the strain, the sheet resistance was partially recovered and stabilized at $0.35 \text{ } \Omega/\square$ with 0% strain. After the first cycle of stretching/releasing, the electrical resistance was restored to a stable value, with a resistance increase of $\sim 30\%$ under 30% stretching. The stable electrical performance under 30% of strain indicates that it can be intrinsically attributed to the reserved elongation of the hybrid nanowires due to their flexible and curved structures (Figure 3.15a). Moreover, the obvious resistance increase could be caused when strain ratio exceeded 60% due to the partially breaking or cracking of the silver nanoparticle layer on CNT's surface, which can possibly lead to an electrical breakdown. Mechanical breakage of FSCs took place when PDMS was stretched beyond the maximum elongation ratio of 100%. Additional stretch/release cycles in the range of 0-60% were performed to evaluate the reliability of FSCs. For up to 500 repeated stretching cycles, FSCs showed relatively stable sheet resistance ($0.35 \text{ } \Omega/\square$ at the strain of 0%) with a small variation of less than 8% (Figure 3.17b), with no observed indication of failure. These results demonstrate good reliability and stable electro-mechanical properties of the hybrid nanowire based FSCs when compared to other reported CNT and silver nanowire composites[99]–[101]. For example, many of single-walled carbon nanotube (SWCNT) flexible composites showed order-of-magnitude higher initial resistivity and significant increase of resistance after the first stretching cycle due to the large contact resistivity of individual CNTs[99], [100]. Furthermore, the stretchable electrode based on a silver nanowire-polymer composite presented a poor electro-mechanical stability for stretching (1000 times increase of resistivity at the strain of 80%) and low reliability under strain cycles (3 times increase of resistivity at the first 500 cycles with a strain of 30%) due to the detachment of the nanowire contacts and crack formation during stretching[101].

In order to understand the electrical conduction mechanism of FSCs, morphology analysis of the multi-functionalized CNT based hybrid nanowires before and under stretching was performed by scanning electron microscopy (SEM), with the results shown in Figure 3.18a-b. It can be seen that the multi-functionalized CNT based hybrid nanowires still retain a complete silver nanoparticle coating layer after removing both the silica and APTES layer by HF etching. Subsequently when the FSCs were stretched, the original bent hybrid nanowires were straightened towards the direction of the tensile strain. The bent structure of the hybrid

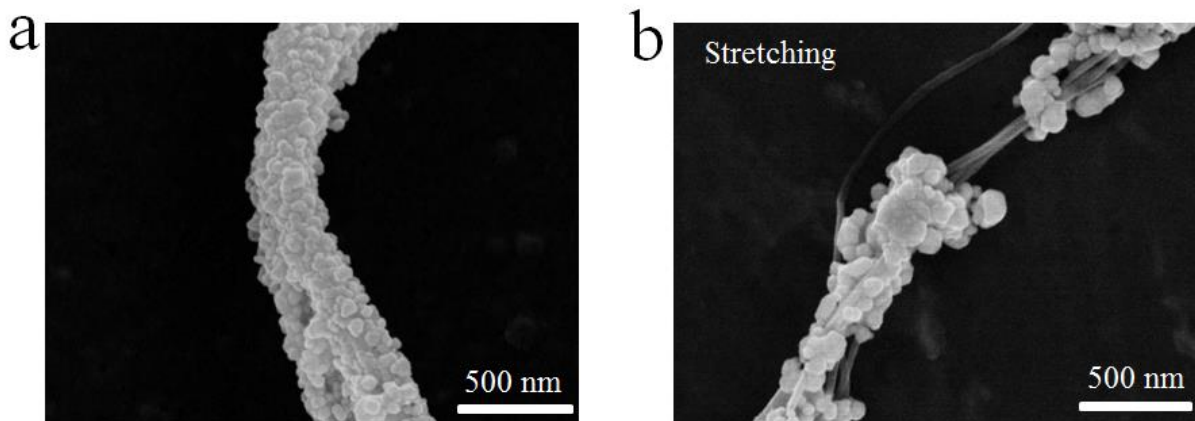


Figure 3.18: (a) SEM images of the multi-functionalized CNT based hybrid nanowire after HF etching. The hybrid nanowire still holds a complete silver-nanoparticle layer even though some defects were identified. (b) When a small tensile strain (<30%) was applied, the original bent hybrid nanowires was firstly straighten towards the direction of strain, which showed stable electro-mechanical properties of FSCs within 30% strain. With the strain ratio further increasing till 60%, the silver-nanoparticles layer was broken to short pieces, and they had a shift along the axis of CNTs towards the direction of stretching. The interspaces between each piece prevent further structural damage. Moreover, it can be seen that CNT bundles have a close connection with each silver piece after removing APTES and silica layers and act as bridges to provide more pathways for electron transmission.

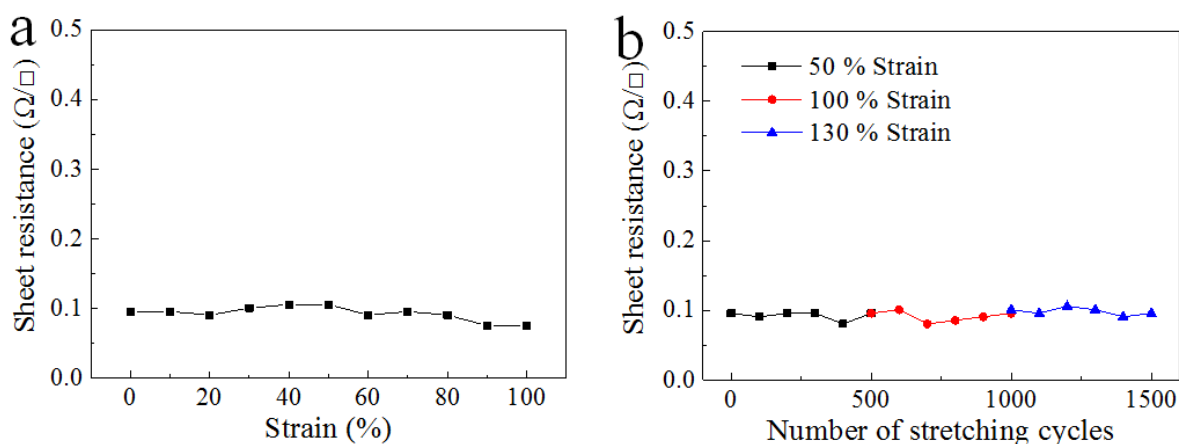


Figure 3.19: (a) Resistance change of FSCs on the pre-stretched silicon rubber substrate as a function of applied strain. FSCs showed a highly stable sheet resistance ($\sim 0.1 \Omega/\square$) with a small variation of 7% under 100% stretching. Such stable electro-mechanical properties are attributed to the flexibility of the hybrid nanowires. (b) Resistance results of FSCs on the pre-stretched silicon rubber substrate under repeated stretch and release cycles. During the first 500 cycles, the FSCs were stretched with 50% strain and showed a constant resistance ($R/R_0 \approx 1$ at 0% strain), and for the second 500 cycles, FSCs were stretched to an increased strain ratio of 100% and also showed a stable resistance ($R/R_0 \approx 1$ at 0% strain). At the last 500 cycles, FSCs were stretched with a further increased strain of 130%. The resistance still remained stable with a slight increase of 10% ($R/R_0 = 1.1$ at 0% strain).

nanowires helps to maintain a stable electrical resistance of FSCs within a tensile strain of 30%. With further increase of the tensile strain, the original silver nanoparticles layer was broken into short pieces that had moved along the axis of CNTs towards the direction of tensile strain. The breakage of the silver nanoparticle coating layer led to the increase of resistance beyond a strain ratio of 30%. However, more stretch/release cycles did not cause a complete failure or any further resistance increase in the FSCs. It has been found that these short pieces were still attached to the surface of CNTs after stretching, instead of forming individual nanoparticles. Under large strains, the interspaces between each piece had enough room for their movement, preventing further structural damage. Moreover, the network of CNTs still acted like bridges to connect each piece and provide more pathways for electron transmission. This also partially helped to maintain a low resistance of FSCs at larger strains.

3.4 Improved stretchability and reliability of FSCs

To further improve the electrical stability as well as the stretchability, FSCs were transferred onto a pre-stretched PDMS substrate with a tensile strain of 100%. The sheet resistance of the sample was evaluated and shown in Figure 3.19a. It has been found that FSCs showed a stable sheet resistance ($\sim 0.1 \Omega/\square$) with a small variation of 7% under 100% stretching. This result represents a three-fold of improvement in the electro-mechanical properties of FSCs compared to the previous case when the non-pre-stretched FSPC was strained to 30%. Such stable electro-mechanical performance of FSCs is attributed to the highly flexible structure of the hybrid nanowires and protection of PDMS. Further increase of the pre-strain ratio of the PDMS substrate could result in an even more stable electrical performance and improved stretchability. Moreover, the maximum strain was increased to 800% before causing mechanical breakdown of pre-stretched FSCs due to the use of even softer PDMS (ELASTOSIL®RT 4600A/B).

The electrical reliability test was also carried out on the high precision load/displacement measurement machine with a strain rate of 5 mm/s to evaluate the reliability of FSCs on the pre-stretched silicon rubber substrate, with the results shown in Figure 3.19b. During the first 500 cycles, the FSCs were stretched with 50% strain and showed a constant resistance ($R/R_0 \approx 1$ at 0% strain), and for the second 500 cycles, FSCs were stretched to an increased strain ratio of 100% and also showed a stable resistance ($R/R_0 \approx 1$ at 0% strain). At the last 500 cycles, FSCs were stretched with a further increased strain of 130%. The resistance still remained stable with a slight increase of 10% ($R/R_0 = 1.1$ at 0% strain). Such stable electrical performance of the FSCs is attributed to the intrinsic flexibility of the multi-functionalized CNT based hybrid nanowires and the sufficient protection from the PDMS layer. These results indicate the stable and superior electro-mechanical properties of FSCs under larger stretching ratios compared to other reports on elastic conductors in literature[72][100]–[109]. For example, electronic whiskers based on patterned carbon nanotube and silver nanoparticle show a three times increase in resistance at a small strain of 2.4% due to the increase of distance between individual silver nanoparticles[102]. Pre-stretched PDMS substrate with copper coating suffer poor reliability caused by cracks formation during repeated stretching/releasing cycles[92]. Stretchable conductors comprising of silver nanowires suffer

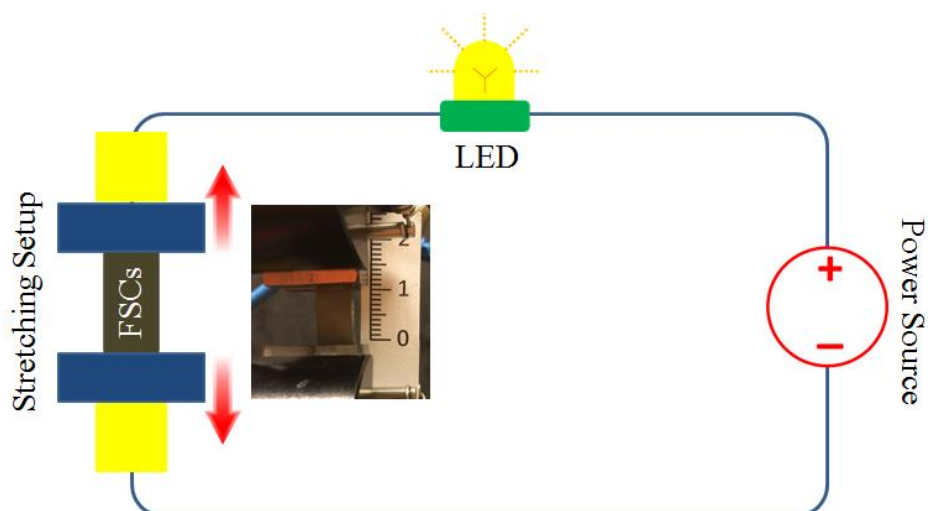


Figure 3.20: Schematic drawing of the LED circuit for the stretching demonstration. FSCs were fixed between two clamps of the stretching setup and connected with a commercial power source and LED. The working voltage of the LED is 2V.

an irreversible increase of resistance after the first stretch/release cycle due to the rigid structure of silver nanowires, and they also show poor electro-mechanical performance and low electrical stability[101], [103]. Many metal/polymer composite films exhibit lower reliability than the hybrid nanowire based FSCs[104]–[106]. A variety of reported FSCs comprising of CNTs and elastic polymers show resistance that are orders of magnitude higher than that of multi-functionalized CNT based hybrid nanowires based FSCs[100], [107]–[109].

A LED demonstrator was built to illustrate the resistance change of the FSCs on a pre-stretched PDMS substrate, which was stretched at different strain ratios with the assist of high precision load/displacement measurement machine. Figure 3.20 shows the schematic of the circuit of the LED demonstrator comprising of the conductive trace fixed between two clamps of the load/displacement machine, an LED and power source. The conductive trace was cyclically stretched with a strain rate of 5mm/s. The working voltage of the LED is 2V.

The lit images and the surface morphology of the conductive trace are shown in Figure 3.21a-b. Compared to the initial light state (strain = 0%), the LED remained the same brightness under different strain ratios (50% and 100%). Due to the prestretched PDMS substrate, the surface of conductor showed some wrinkles running opposite to the direction of stretching in the initial state (0% strain) and these started to disappear as the percentage strain was increased. Those wrinkles would raise challenges to the direct connection between conductive wires and functional devices. Therefore, it is essential to combine both non-prestretched and prestretched FSCs for meeting various requirements of real applications. The sufficient protection from the PDMS layer prevented the conductive layer from getting any structural damage.

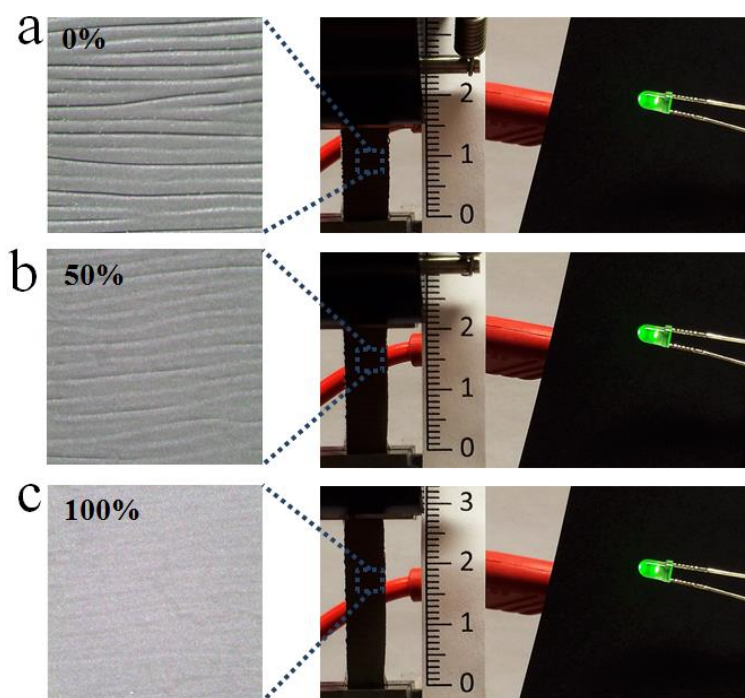


Figure 3.21: (a-b) LED demonstrator and surface morphology change of FSCs under stretching (see video S1). Compared to the initial light state (strain = 0%), the LED demonstrator remained the same illumination intensity under different stretching ratios (50% and 100%). The optical image of the conductor surface showed that some wrinkles appear against the direction of stretching at the initial state and disappear as the strain decreased. The good reliability of the FSCs on the pre-stretched substrate was attributed to the excellent flexibility of hybrid nanowires and the sufficient protection from PDMS.

Chapter 4

Conclusions and Outlook

The thesis focuses on developing flexible and scalable chemical approaches to functionalize CNMs. According to the bonding difference between CNMs and the functional components, the functionalization methods can be divided into two groups, which are covalent functionalization and non-covalent functionalization.

Covalent functionalization of the CNM's surface is based on reactions with the oxygen-containing groups bonded directly to the π -conjugated skeleton of the CNMs. The first part of work introduced an efficient surface activation process using simultaneous oxidation and ultrasonication to activate the CNT surface. It shows much higher activation efficiency than the traditional acid etching processes. Self-assembly of silver nanoparticles on CNT surface were achieved in a complex silver coating solution where a stable silver nanoparticle deposition speed was maintained due to the sustained ion release property of metal-ion chelates. As a result, finely grained and uniform silver nanoparticles were successfully deposited on the surface of activated CNTs. The covalent functionalization process has great potential for the mass production of metal particle supported CNMs due to the low costs, simplicity, and good compatibility. The second part of work focuses on the fabrication of free-standing GBFs via self-assembly and functionalization to improve GBF's heat spreading performance. The self-assembly process are regulated through controlling the individual graphene lateral size and concentration of the dispersion to obtain smooth and wrinkle-free GBF films. The as-fabricated GBFs show good flexibility, strong mechanical strength, and especially a very high in-plane thermal conductivity. To minimize thermal interface resistance between substrates and the GBF, the surface of GBFs was functionalized by the silane coupling agent which can build covalent bonds between graphene basal plane and the substrate surface. Thermal testing results show efficient cooling performance of the functionalized GBF which lower the working temperature of the hotspot for 11 °C. These results could offer potential solutions for the thermal management of high power devices.

Non-covalent functionalization utilizes various functional molecules or active species as assembly mediators to functionalize the surface of CNMs via non-covalent interactions, such as hydrophobic, π - π stacking, and wrapping interaction. The functional mediators would then act as binding points for anchoring other molecules or nanomaterials. Here, multi-functionalized CNT based hybrid nanowires were synthesized with different functional materials on the surface of CNTs to produce a metal nanoparticle coating layer and form uniform dispersions whilst possessing the CNT's original structural integrity and high flexibility. Non-covalent functionalization of CNT was realized through polymer wrapping. The targeted wrapping of APTES and silica layers on the surface of CNT enabled the formation of homogeneous dispersions in various polar solvents, and also facilitated the following silver nanoparticles deposition.

The synthesized multi-functionalized CNT based hybrid nanowires possess a highly conductive and flexible structure which can retain stable electrical and mechanical

performances under significant structural deformation. It shows great potential in the application of FSCs. The good dispersability of the hybrid nanowire in polar solvents facilitates directly making FSCs with fine patterns by existing patterning processes. FSCs fabricated from the hybrid nanowires show a constant electrical resistance under repeated bending cycles and also a low and stable sheet resistance for strains up to 30%, which is orders of magnitude lower than that of pure CNT samples. Further improved stretchability and electro-mechanical properties were achieved with a pre-strained PDMS substrate. Repeated deformation tests demonstrate the high reliability of FSCs. These results indicate the great potential of hybrid nanowires in many applications including wearable flexible displays, stretchable energy generators and capacitors, electronic skins, and deformable sensor and actuator applications.

Future work will be focused on improving the current functionalization processes of CNMs for diverse applications. For example, the surface activation processes presented in the thesis may bring adverse effects to CNT's structure and properties, such as decreased aspect ratio, poor mechanical strength and low electrical conductivity. To minimize such effects, the oxidation degree of CNTs needs to be regulated through controlling the activation time and temperature. The fabricated metal coated CNT hybrids have the advantages of light weight and low costs, which can be used for replacing the traditional pure metal fillers in the conductive adhesive. To meet the requirement of the adhesive for high electrical and thermal conductivity, the metal coverage ratio on the surface of CNTs needs to be improved till to form complete metal shells. The second part of future work is to improve the functionalization of GBFs. The original APTES functionalization process requires the usage of GO to build covalent bonds with the silica substrate. However, it is well-known that GO is a poor media for phonon transfer due to the effect of oxygen. Therefore, new functional agents need to be explored to replace APTES and GO to improve the heat dissipating performance of GBFs. Finally, the developed multi-functionalized CNT based hybrid nanowires have demonstrated good flexibility and high electrical conductivity. More applications using the hybrid nanowires will be investigated, such as electrodes, sensors, catalysts, thermal management and biomedical materials.

Acknowledgements

I would like to thank my supervisor and examiner Prof. Johan Liu for giving me the opportunity to work in such a challenging and exciting research area, and particularly, for his continuous support and advices. Special thanks give to my co-supervisors Dr. Lilei Ye and Dr. Murali Murugesan for their valuable inspiring scientific discussions during whole of my various projects.

Also, I want to express my thanks to Dr. Björn Carlberg for giving me help on managing the chemistry laboratory and many advices at the beginning of my research life. I also want to thank Dr Si Chen for his precious knowledge on packaging materials and machine support.

I would like to thank Di Jiang for his collaboration and many great discussions on our research topics.

Also I would like to thank to all my former and present colleagues at the BioNano Systems Laboratory: Carl Zandén, Wei Mu, Michel Edwards, Yong Zhang, Shuangxi Sun, Yifeng Fu, Changhong Zhao, Nikolaos Logothetis, Majid Kabiri Samani, Zhili Hu, Xin Luo, and many others for their friendship, support, discussion and collaboration.

Many thanks are given to Svante Pålsson, Christer Andersson, Kaija Matikainen, Göran Petersson who work at the Nanofabrication Laboratory in MC2 for their invaluable support on chemical order, laboratory safety and instrument maintenance.

Last but not least, I would like to thank my family for their unconditional love and encouragement throughout my research.

Bibliography

- [1] N. Ferrer-Anglada, V. Gomis, Z. El-Hachemi, U. D. Weglikovska, M. Kaempgen, and S. Roth, “Carbon nanotube based composites for electronic applications: CNT–conducting polymers, CNT–Cu,” *Phys. Status Solidi A*, vol. 203, no. 6, pp. 1082–1087, 2006.
- [2] L. Aryasomayajula and K.-J. Wolter, “Carbon Nanotube Composites for Electronic Packaging Applications: A Review,” *J. Nanotechnol.*, vol. 2013, p. e296517, May 2013.
- [3] K. Zhang, M. M. F. Yuen, N. Wang, J. Y. Miao, D. G. W. Xiao, and H. B. Fan, “Thermal interface material with aligned CNT and its application in HB-LED packaging,” in *Electronic Components and Technology Conference, 2006. Proceedings. 56th*, 2006, p. 6 pp.–.
- [4] Z. Gao, Y. Zhang, Y. Fu, M. Yuen, and J. Liu, “Graphene heat spreader for thermal management of hot spots in electronic packaging,” in *2012 18th International Workshop on Thermal Investigations of ICs and Systems (THERMINIC)*, 2012, pp. 1–4.
- [5] K. M. F. Shahil and A. A. Balandin, “Thermal properties of graphene and multilayer graphene: Applications in thermal interface materials,” *Solid State Commun.*, vol. 152, no. 15, pp. 1331–1340, 2012.
- [6] L. Dai, “Functionalization of Graphene for Efficient Energy Conversion and Storage,” *Acc. Chem. Res.*, vol. 46, no. 1, pp. 31–42, 2013.
- [7] J. Hou, Y. Shao, M. W. Ellis, R. B. Moore, and B. Yi, “Graphene-based electrochemical energy conversion and storage: fuel cells, supercapacitors and lithium ion batteries,” *Phys. Chem. Chem. Phys.*, vol. 13, no. 34, p. 15384, 2011.
- [8] H.-J. Choi, S.-M. Jung, J.-M. Seo, D. W. Chang, L. Dai, and J.-B. Baek, “Graphene for energy conversion and storage in fuel cells and supercapacitors,” *Nano Energy*, vol. 1, no. 4, pp. 534–551, 2012.
- [9] L. Yin, Y. Wang, G. Pang, Y. Koltypin, and A. Gedanken, “Sonochemical Synthesis of Cerium Oxide Nanoparticles—Effect of Additives and Quantum Size Effect,” *J. Colloid Interface Sci.*, vol. 246, no. 1, pp. 78–84, 2002.
- [10] S. Qiu, Z. Zhou, J. Dong, and G. Chen, “Preparation of Ni Nanoparticles and Evaluation of Their Tribological Performance as Potential Additives in Oils,” *J. Tribol.*, vol. 123, no. 3, pp. 441–443, 1999.
- [11] Z. Liu, X. Y. Ling, X. Su, and J. Y. Lee, “Carbon-Supported Pt and PtRu Nanoparticles as Catalysts for a Direct Methanol Fuel Cell,” *J. Phys. Chem. B*, vol. 108, no. 24, pp. 8234–8240, 2004.
- [12] J. Wang and M. Musameh, “Carbon nanotube screen-printed electrochemical sensors,” *The Analyst*, vol. 129, no. 1, p. 1, 2004.
- [13] J. T. Robinson, F. K. Perkins, E. S. Snow, Z. Wei, and P. E. Sheehan, “Reduced Graphene Oxide Molecular Sensors,” *Nano Lett.*, vol. 8, no. 10, pp. 3137–3140, 2008.
- [14] X. Sun, Z. Liu, K. Welsher, J. T. Robinson, A. Goodwin, S. Zaric, and H. Dai, “Nano-graphene oxide for cellular imaging and drug delivery,” *Nano Res.*, vol. 1, no. 3, pp. 203–212, Aug. 2008.

- [15] Z. Liu, S. Tabakman, K. Welsher, and H. Dai, "Carbon nanotubes in biology and medicine: In vitro and in vivo detection, imaging and drug delivery," *Nano Res.*, vol. 2, no. 2, pp. 85–120, Mar. 2010.
- [16] F. Chen, Z.-C. Wang, and C.-J. Lin, "Preparation and characterization of nano-sized hydroxyapatite particles and hydroxyapatite/chitosan nano-composite for use in biomedical materials," *Mater. Lett.*, vol. 57, no. 4, pp. 858–861, 2002.
- [17] P. Gatenholm and D. Klemm, "Bacterial Nanocellulose as a Renewable Material for Biomedical Applications," *MRS Bull.*, vol. 35, no. 03, pp. 208–213, 2010.
- [18] J. Weiss, P. Takhistov, and D. J. McClements, "Functional Materials in Food Nanotechnology," *J. Food Sci.*, vol. 71, no. 9, pp. R107–R116, 2006.
- [19] H. J. Fecht and K. Brühne, *Carbon-based Nanomaterials and Hybrids: Synthesis, Properties, and Commercial Applications*. CRC Press, 2014.
- [20] K. Ariga, M. Li, G. J. Richards, and J. P. Hill, "Nanoarchitectonics: A Conceptual Paradigm for Design and Synthesis of Dimension-Controlled Functional Nanomaterials," *J. Nanosci. Nanotechnol.*, vol. 11, no. 1, pp. 1–13, Jan. 2011.
- [21] Y. Zhao, J. Liu, Y. Hu, H. Cheng, C. Hu, C. Jiang, L. Jiang, A. Cao, and L. Qu, "Highly Compression-Tolerant Supercapacitor Based on Polypyrrole-mediated Graphene Foam Electrodes," *Adv. Mater.*, vol. 25, no. 4, pp. 591–595, 2013.
- [22] Y. Hu, O. A. Shenderova, Z. Hu, C. W. Padgett, and D. W. Brenner, "Carbon nanostructures for advanced composites," *Rep. Prog. Phys.*, vol. 69, no. 6, p. 1847, Jun. 2006.
- [23] V. S. Vavilov, "The properties of natural and synthetic diamond," *Phys.-Uspekhi*, vol. 36, no. 11, p. 1083, Nov. 1993.
- [24] N. Park and J. Ihm, "Electronic structure and mechanical stability of the graphitic honeycomb lattice," *Phys. Rev. B*, vol. 62, no. 11, pp. 7614–7618, 2000.
- [25] W. J. Bartz, "Solid lubricant additives—effect of concentration and other additives on anti-wear performance," *Wear*, vol. 17, no. 5–6, pp. 421–432, 1971.
- [26] B. C. Thompson and J. M. J. Fréchet, "Polymer–Fullerene Composite Solar Cells," *Angew. Chem. Int. Ed.*, vol. 47, no. 1, pp. 58–77, 2008.
- [27] S. Margadonna and K. Prassides, "Recent Advances in Fullerene Superconductivity," *J. Solid State Chem.*, vol. 168, no. 2, pp. 639–652, 2002.
- [28] T. Wharton and L. J. Wilson, "Highly-Iodinated Fullerene as a Contrast Agent For X-ray Imaging," *Bioorg. Med. Chem.*, vol. 10, no. 11, pp. 3545–3554, 2002.
- [29] R. Singh and J. W. Lillard Jr., "Nanoparticle-based targeted drug delivery," *Exp. Mol. Pathol.*, vol. 86, no. 3, pp. 215–223, 2009.
- [30] B. G. Demczyk, Y. M. Wang, J. Cumings, M. Hetman, W. Han, A. Zettl, and R. O. Ritchie, "Direct mechanical measurement of the tensile strength and elastic modulus of multiwalled carbon nanotubes," *Mater. Sci. Eng. A*, vol. 334, no. 1–2, pp. 173–178, 2002.
- [31] K. I. Bolotin, K. J. Sikes, Z. Jiang, M. Klima, G. Fudenberg, J. Hone, P. Kim, and H. L. Stormer, "Ultrahigh electron mobility in suspended graphene," *Solid State Commun.*, vol. 146, no. 9–10, pp. 351–355, 2008.

- [32] F. Kreupl, A. P. Graham, G. S. Duesberg, W. Steinhögl, M. Liebau, E. Unger, and W. Hönlein, "Carbon nanotubes in interconnect applications," *Microelectron. Eng.*, vol. 64, no. 1–4, pp. 399–408, 2002.
- [33] A. A. Balandin, S. Ghosh, W. Bao, I. Calizo, D. Teweldebrhan, F. Miao, and C. N. Lau, "Superior Thermal Conductivity of Single-Layer Graphene," *Nano Lett.*, vol. 8, no. 3, pp. 902–907, 2008.
- [34] "Continuous, Highly Flexible, and Transparent Graphene Films by Chemical Vapor Deposition for Organic Photovoltaics - ACS Nano (ACS Publications)." [Online]. Available: <http://pubs.acs.org/doi/abs/10.1021/nn901587x>. [Accessed: 05-Jul-2015].
- [35] "High Mobility, Printable, and Solution-Processed Graphene Electronics - Nano Letters (ACS Publications)." [Online]. Available: <http://pubs.acs.org/doi/abs/10.1021/nl9028736>. [Accessed: 05-Jul-2015].
- [36] T. S. Sreepasad, S. M. Maliyekkal, K. P. Lisha, and T. Pradeep, "Reduced graphene oxide–metal/metal oxide composites: Facile synthesis and application in water purification," *J. Hazard. Mater.*, vol. 186, no. 1, pp. 921–931, 2011.
- [37] A. M. K. Esawi and M. M. Farag, "Carbon nanotube reinforced composites: Potential and current challenges," *Mater. Des.*, vol. 28, no. 9, pp. 2394–2401, 2007.
- [38] "Flexible energy storage devices based on graphene paper - Energy & Environmental Science (RSC Publishing) DOI:10.1039/C0EE00640H." [Online]. Available: <http://pubs.rsc.org/en/content/articlehtml/2011/ee/c0ee00640h>. [Accessed: 05-Jul-2015].
- [39] X. Li, Y. Qin, S. T. Picraux, and Z.-X. Guo, "Noncovalent assembly of carbon nanotube-inorganic hybrids," *J. Mater. Chem.*, vol. 21, no. 21, p. 7527, 2011.
- [40] S. Förster and T. Plantenberg, "From Self-Organizing Polymers to Nanohybrid and Biomaterials," *Angew. Chem. Int. Ed.*, vol. 41, no. 5, pp. 688–714, 2002.
- [41] J.-H. Yang, Y.-S. Han, M. Park, T. Park, S.-J. Hwang, and J.-H. Choy, "New Inorganic-Based Drug Delivery System of Indole-3-Acetic Acid-Layered Metal Hydroxide Nanohybrids with Controlled Release Rate," *Chem. Mater.*, vol. 19, no. 10, pp. 2679–2685, 2007.
- [42] Y. Wang, G. Ouyang, J. Zhang, and Z. Wang, "A DNA-templated catalyst: the preparation of metal-DNA nanohybrids and their application in organic reactions," *Chem. Commun.*, vol. 46, no. 42, p. 7912, 2010.
- [43] K.-Y. Chun, Y. Oh, J. Rho, J.-H. Ahn, Y.-J. Kim, H. R. Choi, and S. Baik, "Highly conductive, printable and stretchable composite films of carbon nanotubes and silver," *Nat. Nanotechnol.*, vol. 5, no. 12, pp. 853–857, 2010.
- [44] F. He, J. Fan, D. Ma, L. Zhang, C. Leung, and H. L. Chan, "The attachment of Fe₃O₄ nanoparticles to graphene oxide by covalent bonding," *Carbon*, vol. 48, no. 11, pp. 3139–3144, 2010.
- [45] E. Antolini, "Carbon supports for low-temperature fuel cell catalysts," *Appl. Catal. B Environ.*, vol. 88, no. 1–2, pp. 1–24, 2009.
- [46] S.-F. Zheng, J.-S. Hu, L.-S. Zhong, W.-G. Song, L.-J. Wan, and Y.-G. Guo, "Introducing Dual Functional CNT Networks into CuO Nanomicrospheres toward Superior Electrode Materials for Lithium-Ion Batteries," *Chem. Mater.*, vol. 20, no. 11, pp. 3617–3622, 2008.

- [47] X. Fu, H. Yu, F. Peng, H. Wang, and Y. Qian, "Facile preparation of RuO₂/CNT catalyst by a homogenous oxidation precipitation method and its catalytic performance," *Appl. Catal. Gen.*, vol. 321, no. 2, pp. 190–197, 2007.
- [48] J. Guerra and M. A. Herrero, "Hybrid materials based on Pd nanoparticles on carbon nanostructures for environmentally benign C-C coupling chemistry," *Nanoscale*, vol. 2, no. 8, pp. 1390–1400, Aug. 2010.
- [49] G. G. Wildgoose, C. E. Banks, and R. G. Compton, "Metal nanoparticles and related materials supported on carbon nanotubes: methods and applications," *Small Weinh. Bergstr. Ger.*, vol. 2, no. 2, pp. 182–193, Feb. 2006.
- [50] V. Georgakilas, D. Gournis, V. Tzitzios, L. Pasquato, D. M. Guldi, and M. Prato, "Decorating carbon nanotubes with metal or semiconductor nanoparticles," *J. Mater. Chem.*, vol. 17, no. 26, pp. 2679–2694, Jun. 2007.
- [51] X. Peng, J. Chen, J. A. Misewich, and S. S. Wong, "Carbon nanotube–nanocrystal heterostructures," *Chem. Soc. Rev.*, vol. 38, no. 4, pp. 1076–1098, Mar. 2009.
- [52] N. T. Nikolaos Karousis, "Current progress on the chemical modification of carbon nanotubes," *Chem. Rev.*, vol. 110, no. 9, pp. 5366–97, 2010.
- [53] V. N. Khabashesku, "Covalent functionalization of carbon nanotubes: synthesis, properties and applications of fluorinated derivatives," *Russ. Chem. Rev.*, vol. 80, no. 8, p. 705, Aug. 2011.
- [54] J. Yun, J. S. Im, and H.-I. Kim, "Effect of oxygen plasma treatment of carbon nanotubes on electromagnetic interference shielding of polypyrrole-coated carbon nanotubes," *J. Appl. Polym. Sci.*, vol. 126, no. S2, pp. E39–E47, 2012.
- [55] M. N. Tchoul, W. T. Ford, G. Lolli, D. E. Resasco, and S. Arepalli, "Effect of Mild Nitric Acid Oxidation on Dispersability, Size, and Structure of Single-Walled Carbon Nanotubes," *Chem. Mater.*, vol. 19, no. 23, pp. 5765–5772, 2007.
- [56] M. Zhang, L. Su, and L. Mao, "Surfactant functionalization of carbon nanotubes (CNTs) for layer-by-layer assembling of CNT multi-layer films and fabrication of gold nanoparticle/CNT nanohybrid," *Carbon*, vol. 44, no. 2, pp. 276–283, 2006.
- [57] Y.-L. Zhao and J. F. Stoddart, "Noncovalent Functionalization of Single-Walled Carbon Nanotubes," *Acc. Chem. Res.*, vol. 42, no. 8, pp. 1161–1171, 2009.
- [58] M. J. O'Connell, P. Boul, L. M. Ericson, C. Huffman, Y. Wang, E. Haroz, C. Kuper, J. Tour, K. D. Ausman, and R. E. Smalley, "Reversible water-solubilization of single-walled carbon nanotubes by polymer wrapping," *Chem. Phys. Lett.*, vol. 342, no. 3–4, pp. 265–271, 2001.
- [59] A. N. Enyashin, S. Gemming, and G. Seifert, "DNA-wrapped carbon nanotubes," *Nanotechnology*, vol. 18, no. 24, p. 245702, Jun. 2007.
- [60] L. Jiang, L. Gao, and J. Sun, "Production of aqueous colloidal dispersions of carbon nanotubes," *J. Colloid Interface Sci.*, vol. 260, no. 1, pp. 89–94, 2003.
- [61] T. J. Simmons, J. Bult, D. P. Hashim, R. J. Linhardt, and P. M. Ajayan, "Noncovalent Functionalization as an Alternative to Oxidative Acid Treatment of Single Wall Carbon Nanotubes with Applications for Polymer Composites," *ACS Nano*, vol. 3, no. 4, pp. 865–870, 2009.
- [62] J. H. T. Luong, S. Hrapovic, D. Wang, F. Bensebaa, and B. Simard, "Solubilization of Multiwall Carbon Nanotubes by 3-Aminopropyltriethoxysilane Towards the Fabrication

- of Electrochemical Biosensors with Promoted Electron Transfer,” *Electroanalysis*, vol. 16, no. 1–2, pp. 132–139, 2004.
- [63] W. M. Daoush, B. K. Lim, C. B. Mo, D. H. Nam, and S. H. Hong, “Electrical and mechanical properties of carbon nanotube reinforced copper nanocomposites fabricated by electroless deposition process,” *Mater. Sci. Eng. A*, vol. 513–514, pp. 247–253, 2009.
- [64] J. H. Byeon and J. Hwang, “Morphology of metallic nanoparticles as a function of deposition time in electroless deposition of metal on multi-walled carbon nanotubes,” *Surf. Coat. Technol.*, vol. 203, no. 3–4, pp. 357–363, 2008.
- [65] A. Jorio, M. A. Pimenta, A. G. S. Filho, R. Saito, G. Dresselhaus, and M. S. Dresselhaus, “Characterizing carbon nanotube samples with resonance Raman scattering,” *New J. Phys.*, vol. 5, no. 1, p. 139, Oct. 2003.
- [66] S. K. Choi, K.-Y. Chun, and S.-B. Lee, “Selective decoration of silver nanoparticles on the defect sites of single-walled carbon nanotubes,” *Diam. Relat. Mater.*, vol. 18, no. 4, pp. 637–641, 2009.
- [67] M. Inagaki, R. Tashiro, Y. Washino, and M. Toyoda, “Exfoliation process of graphite via intercalation compounds with sulfuric acid,” *J. Phys. Chem. Solids*, vol. 65, no. 2–3, pp. 133–137, 2004.
- [68] A. Cao, C. Xu, J. Liang, D. Wu, and B. Wei, “X-ray diffraction characterization on the alignment degree of carbon nanotubes,” *Chem. Phys. Lett.*, vol. 344, no. 1–2, pp. 13–17, 2001.
- [69] Y. Sun and Y. Xia, “Shape-Controlled Synthesis of Gold and Silver Nanoparticles,” *Science*, vol. 298, no. 5601, pp. 2176–2179, Dec. 2002.
- [70] S. S. Bale, P. Asuri, S. S. Karajanagi, J. S. Dordick, and R. S. Kane, “Protein-Directed Formation of Silver Nanoparticles on Carbon Nanotubes,” *Adv. Mater.*, vol. 19, no. 20, pp. 3167–3170, 2007.
- [71] M. Lelental, “Dimethylamine Borane as the Reducing Agent in Electroless Plating Systems,” *J. Electrochem. Soc.*, vol. 120, no. 12, pp. 1650–1654, Jan. 1973.
- [72] Z. Gao, Y. Zhang, Y. Fu, M. M. F. Yuen, and J. Liu, “Thermal chemical vapor deposition grown graphene heat spreader for thermal management of hot spots,” *Carbon*, vol. 61, pp. 342–348, 2013.
- [73] K. M. F. Shahil and A. A. Balandin, “Graphene–Multilayer Graphene Nanocomposites as Highly Efficient Thermal Interface Materials,” *Nano Lett.*, vol. 12, no. 2, pp. 861–867, 2012.
- [74] S. H. Aboutalebi, M. M. Gudarzi, Q. B. Zheng, and J.-K. Kim, “Spontaneous Formation of Liquid Crystals in Ultralarge Graphene Oxide Dispersions,” *Adv. Funct. Mater.*, vol. 21, no. 15, pp. 2978–2988, 2011.
- [75] J. H. Byeon and J. Hwang, “Morphology of metallic nanoparticles as a function of deposition time in electroless deposition of metal on multi-walled carbon nanotubes,” *Surf. Coat. Technol.*, vol. 203, no. 3–4, pp. 357–363, 2008.
- [76] X. Ma, N. Lun, and S. Wen, “Formation of gold nanoparticles supported on carbon nanotubes by using an electroless plating method,” *Diam. Relat. Mater.*, vol. 14, no. 1, pp. 68–73, 2005.

- [77] L. Zhao and L. Gao, "Stability of multi-walled carbon nanotubes dispersion with copolymer in ethanol," *Colloids Surf. Physicochem. Eng. Asp.*, vol. 224, no. 1–3, pp. 127–134, 2003.
- [78] Y. Yamada and K. Yano, "Synthesis of monodispersed super-microporous/mesoporous silica spheres with diameters in the low submicron range," *Microporous Mesoporous Mater.*, vol. 93, no. 1–3, pp. 190–198, 2006.
- [79] Z. Xiu, Y. Wu, X. Hao, and L. Zhang, "Fabrication of SiO₂@Ag@SiO₂ core-shell microspheres and thermal stability investigation," *Colloids Surf. Physicochem. Eng. Asp.*, vol. 386, no. 1–3, pp. 135–140, 2011.
- [80] F. Tang, L. Li, and D. Chen, "Mesoporous Silica Nanoparticles: Synthesis, Biocompatibility and Drug Delivery," *Adv. Mater.*, vol. 24, no. 12, pp. 1504–1534, 2012.
- [81] S. K. Choi, K.-Y. Chun, and S.-B. Lee, "Selective decoration of silver nanoparticles on the defect sites of single-walled carbon nanotubes," *Diam. Relat. Mater.*, vol. 18, no. 4, pp. 637–641, 2009.
- [82] X. Ma, N. Lun, and S. Wen, "Formation of gold nanoparticles supported on carbon nanotubes by using an electroless plating method," *Diam. Relat. Mater.*, vol. 14, no. 1, pp. 68–73, 2005.
- [83] S. Guo, J. Li, W. Ren, D. Wen, S. Dong, and E. Wang, "Carbon Nanotube/Silica Coaxial Nanocable as a Three-Dimensional Support for Loading Diverse Ultra-High-Density Metal Nanostructures: Facile Preparation and Use as Enhanced Materials for Electrochemical Devices and SERS," *Chem. Mater.*, vol. 21, no. 11, pp. 2247–2257, 2009.
- [84] Joseph Fjelstad, "Flexible circuitry - technology background and important fundamental issues," *Circuit World*, vol. 25, no. 2, pp. 6–10, 1999.
- [85] J. A. Rogers, Z. Bao, K. Baldwin, A. Dodabalapur, B. Crone, V. R. Raju, V. Kuck, H. Katz, K. Amundson, J. Ewing, and P. Drzaic, "Paper-like electronic displays: Large-area rubber-stamped plastic sheets of electronics and microencapsulated electrophoretic inks," *Proc. Natl. Acad. Sci.*, vol. 98, no. 9, pp. 4835–4840, Apr. 2001.
- [86] S. Park and S. Jayaraman, "Smart Textiles: Wearable Electronic Systems," *MRS Bull.*, vol. 28, no. 08, pp. 585–591, 2003.
- [87] D. J. Lipomi, B. C.-K. Tee, M. Vosgueritchian, and Z. Bao, "Stretchable Organic Solar Cells," *Adv. Mater.*, vol. 23, no. 15, pp. 1771–1775, 2011.
- [88] H. C. Ko, M. P. Stoykovich, J. Song, V. Malyarchuk, W. M. Choi, C.-J. Yu, J. B. Geddes Iii, J. Xiao, S. Wang, Y. Huang, and J. A. Rogers, "A hemispherical electronic eye camera based on compressible silicon optoelectronics," *Nature*, vol. 454, no. 7205, pp. 748–753, 2008.
- [89] R. Carta, P. Jourand, B. Hermans, J. Thon é D. Brosteaux, T. Vervust, F. Bossuyt, F. Axisa, J. Vanfleteren, and R. Puers, "Design and implementation of advanced systems in a flexible-stretchable technology for biomedical applications," *Sens. Actuators Phys.*, vol. 156, no. 1, pp. 79–87, 2009.
- [90] T. Sekitani and T. Someya, "Stretchable, Large-area Organic Electronics," *Adv. Mater.*, vol. 22, no. 20, pp. 2228–2246, 2010.

- [91] M. Gonzalez, F. Axisa, M. V. Bulcke, D. Brosteaux, B. Vandeveldel, and J. Vanfleteren, "Design of metal interconnects for stretchable electronic circuits," *Microelectron. Reliab.*, vol. 48, no. 6, pp. 825–832, 2008.
- [92] X. Wang, H. Hu, Y. Shen, X. Zhou, and Z. Zheng, "Stretchable Conductors with Ultrahigh Tensile Strain and Stable Metallic Conductance Enabled by Prestrained Polyelectrolyte Nanoplatfoms," *Adv. Mater.*, vol. 23, no. 27, pp. 3090–3094, 2011.
- [93] P. Calvert, "Inkjet Printing for Materials and Devices," *Chem. Mater.*, vol. 13, no. 10, pp. 3299–3305, 2001.
- [94] T.-Y. Dong, W.-T. Chen, C.-W. Wang, C.-P. Chen, C.-N. Chen, M.-C. Lin, J.-M. Song, I.-G. Chen, and T.-H. Kao, "One-step synthesis of uniform silver nanoparticles capped by saturated decanoate: direct spray printing ink to form metallic silver films," *Phys. Chem. Chem. Phys.*, vol. 11, no. 29, pp. 6269–6275, Aug. 2009.
- [95] K. Kordás, T. Mustonen, G. Tóth, H. Jantunen, M. Lajunen, C. Soldano, S. Talapatra, S. Kar, R. Vajtai, and P. M. Ajayan, "Inkjet Printing of Electrically Conductive Patterns of Carbon Nanotubes," *Small*, vol. 2, no. 8–9, pp. 1021–1025, 2006.
- [96] J. Wu, M. Agrawal, H. A. Becerril, Z. Bao, Z. Liu, Y. Chen, and P. Peumans, "Organic Light-Emitting Diodes on Solution-Processed Graphene Transparent Electrodes," *ACS Nano*, vol. 4, no. 1, pp. 43–48, 2010.
- [97] L. Hu, H. S. Kim, J.-Y. Lee, P. Peumans, and Y. Cui, "Scalable Coating and Properties of Transparent, Flexible, Silver Nanowire Electrodes," *ACS Nano*, vol. 4, no. 5, pp. 2955–2963, 2010.
- [98] Z. Chen, W. Ren, L. Gao, B. Liu, S. Pei, and H.-M. Cheng, "Three-dimensional flexible and conductive interconnected graphene networks grown by chemical vapour deposition," *Nat. Mater.*, vol. 10, no. 6, pp. 424–428, 2011.
- [99] T. Kim, H. Song, J. Ha, S. Kim, D. Kim, S. Chung, J. Lee, and Y. Hong, "Inkjet-printed stretchable single-walled carbon nanotube electrodes with excellent mechanical properties," *Appl. Phys. Lett.*, vol. 104, no. 11, p. 113103, Mar. 2014.
- [100] T. Sekitani, Y. Noguchi, K. Hata, T. Fukushima, T. Aida, and T. Someya, "A Rubberlike Stretchable Active Matrix Using Elastic Conductors," *Science*, vol. 321, no. 5895, pp. 1468–1472, Dec. 2008.
- [101] S. Yun, X. Niu, Z. Yu, W. Hu, P. Brochu, and Q. Pei, "Compliant Silver Nanowire-Polymer Composite Electrodes for Bistable Large Strain Actuation," *Adv. Mater.*, vol. 24, no. 10, pp. 1321–1327, 2012.
- [102] K. Takei, Z. Yu, M. Zheng, H. Ota, T. Takahashi, and A. Javey, "Highly sensitive electronic whiskers based on patterned carbon nanotube and silver nanoparticle composite films," *Proc. Natl. Acad. Sci. U. S. A.*, vol. 111, no. 5, pp. 1703–1707, Feb. 2014.
- [103] F. Xu and Y. Zhu, "Highly Conductive and Stretchable Silver Nanowire Conductors," *Adv. Mater.*, vol. 24, no. 37, pp. 5117–5122, 2012.
- [104] K.-Y. Chun, Y. Oh, J. Rho, J.-H. Ahn, Y.-J. Kim, H. R. Choi, and S. Baik, "Highly conductive, printable and stretchable composite films of carbon nanotubes and silver," *Nat. Nanotechnol.*, vol. 5, no. 12, pp. 853–857, 2010.
- [105] M. Park, J. Im, M. Shin, Y. Min, J. Park, H. Cho, S. Park, M.-B. Shim, S. Jeon, D.-Y. Chung, J. Bae, J. Park, U. Jeong, and K. Kim, "Highly stretchable electric circuits from a

- composite material of silver nanoparticles and elastomeric fibres,” *Nat. Nanotechnol.*, vol. 7, no. 12, pp. 803–809, 2012.
- [106] Y. Yu, J. Zeng, C. Chen, Z. Xie, R. Guo, Z. Liu, X. Zhou, Y. Yang, and Z. Zheng, “Three-Dimensional Compressible and Stretchable Conductive Composites,” *Adv. Mater.*, vol. 26, no. 5, pp. 810–815, 2014.
- [107] Y. Li and H. Shimizu, “Toward a Stretchable, Elastic, and Electrically Conductive Nanocomposite: Morphology and Properties of Poly[styrene-*b*-(ethylene-co-butylene)-*b*-styrene]/Multiwalled Carbon Nanotube Composites Fabricated by High-Shear Processing,” *Macromolecules*, vol. 42, no. 7, pp. 2587–2593, 2009.
- [108] L. Hu, M. Pasta, F. L. Mantia, L. Cui, S. Jeong, H. D. Deshazer, J. W. Choi, S. M. Han, and Y. Cui, “Stretchable, Porous, and Conductive Energy Textiles,” *Nano Lett.*, vol. 10, no. 2, pp. 708–714, 2010.
- [109] J. Li, L. Liu, D. Zhang, D. Yang, J. Guo, and J. Wei, “Fabrication of polyaniline/silver nanoparticles/multi-walled carbon nanotubes composites for flexible microelectronic circuits,” *Synth. Met.*, vol. 192, pp. 15–22, 2014.

